

1 **Intrinsically aggregation-prone proteins form amyloid-like aggregates and**  
2 **contribute to tissue aging in *C. elegans*.**

3 Huang C. <sup>1</sup>, Wagner-Valladolid S. <sup>3§</sup>, Stephens A. D. <sup>3§</sup>, Jung R. <sup>1</sup>, Poudel C. <sup>3</sup>, Sinnige T. <sup>4</sup>, Lechler M. C. <sup>1,2</sup>,  
4 Schlörit N. <sup>1,2</sup>, Lu M. <sup>3</sup>, Laine R. F. <sup>3,5</sup>, Michel C. H. <sup>3</sup>, Vendruscolo M. <sup>4</sup>, Kaminski C. F. <sup>3</sup>, Kaminski Schierle G.  
5 S. <sup>3\*</sup>, David D. C. <sup>1\*</sup>

6 <sup>1</sup> German Center for Neurodegenerative Diseases (DZNE), 72076 Tübingen, Germany

7 <sup>2</sup> Graduate School of Cellular and Molecular Neuroscience, 72074 Tübingen, Germany

8 <sup>3</sup> Department of Chemical Engineering and Biotechnology, University of Cambridge, Cambridge, CB3 0AS,  
9 UK

10 <sup>4</sup> Department of Chemistry, University of Cambridge, Cambridge, CB2 1EW, UK

11 <sup>5</sup> Present address: Medical Research Council Laboratory for Molecular Cell Biology, University College  
12 London, London, Gower street, WC1E 6BT, United Kingdom

13 <sup>§</sup> These authors contributed equally to this work.

14 \* Co-corresponding authors: [della.david@dzne.de](mailto:della.david@dzne.de) and [gsk20@cam.ac.uk](mailto:gsk20@cam.ac.uk)

15

16 Keywords: Protein aggregation, Aging, Amyloid, *C. elegans*

17

18 **Abstract:**

19 Reduced protein homeostasis leading to increased protein instability is a common molecular feature of  
20 aging, but it remains unclear whether this is a cause or consequence of the aging process. In  
21 neurodegenerative diseases and other amyloidoses, specific proteins self-assemble into amyloid fibrils  
22 and accumulate as pathological aggregates in different tissues. More recently, widespread protein  
23 aggregation has been described during normal aging. Until now, an extensive characterization of the  
24 nature of age-dependent protein aggregation has been lacking. Here, we show that age-dependent  
25 aggregates are rapidly formed by newly synthesized proteins and have an amyloid-like structure  
26 resembling that of protein aggregates observed in disease. We then demonstrate that age-dependent  
27 protein aggregation accelerates the functional decline of different tissues in *C. elegans*. Together, these  
28 findings imply that amyloid-like aggregates contribute to the aging process and therefore could be  
29 important targets for strategies designed to maintain physiological functions in the late stages of life.

30

31

32 **Introduction:**

33 Aging is a gradual decline in physiological functions and organ integrity and indeed diminished physical  
34 capacity and cognitive functions are already apparent before midlife (Belsky et al., 2015). The aging  
35 process greatly enhances the risk for chronic diseases leading to long-term disabilities in the elderly  
36 population and often premature death (Kaeberlein, 2013). A better understanding of what drives aging  
37 and in particular functional decline holds the promise of identifying targets to maintain quality of life  
38 with old age. It is generally agreed that the ultimate root causes of aging occur at the molecular level  
39 (Kaeberlein, 2013). One of the most universal hallmarks of aging is increased protein instability (Golubev,  
40 Hanson, & Gladyshev, 2017; Gorisse et al., 2016). In young individuals, an efficient protein homeostasis

41 (proteostasis) network prevents the accumulation of damaged proteins. However, overwhelming  
42 evidence points to a collapse in the proteostasis network with age and consequently a decline in the  
43 ability to cope with protein physical and chemical instability (Taylor & Dillin, 2011). Still the role of  
44 protein instability in aging is unclear (Finch & Crimmins, 2016; Hekimi, Lapointe, & Wen, 2011).

45 During aging, an important cause of protein instability is cumulative damage through non-enzymatic  
46 posttranslational modifications occurring through reactions with metabolites and reactive oxygen  
47 species (Golubev et al., 2017). Destabilizing mutations, transcriptional and translational inefficacy are  
48 also a significant source of protein instability (Nedialkova & Leidel, 2015; Vermulst et al., 2015). In a  
49 disease context, a specific form of protein instability, namely protein aggregation, is a common feature  
50 of amyloidoses and many neurodegenerative diseases. In these diseases, a specific protein converts from  
51 its native soluble conformation into an insoluble state by self-assembly into a cross- $\beta$  sheet filamentous  
52 structure termed amyloid fibril. Amyloid fibrils accumulate as pathological deposits in a variety of  
53 different tissues. Although most proteins contain amyloid-promoting sequences and form amyloid fibrils  
54 in appropriate conditions *in vitro* (Chiti et al., 1999; Goldschmidt, Teng, Riek, & Eisenberg, 2010), there is  
55 little evidence for this disease-related conformational state in metazoa in the absence of disease. Global  
56 proteomic characterizations of age-dependent protein insolubility, a hallmark of disease-associated  
57 protein aggregation, have been carried out in wild-type *C. elegans* (David et al., 2010; Reis-Rodrigues et  
58 al., 2012; Walther et al., 2015). Several hundred proteins enriched in distinct structural and functional  
59 characteristics were identified that lose their native structure in aged animals and become highly-  
60 insoluble in strong detergents (David et al., 2010; Lechler et al., 2017; Reis-Rodrigues et al., 2012). *In vivo*  
61 data demonstrate that these proteins accumulate in solid/immobile structures in aged animals.  
62 However, until now it is not known whether these age-dependent protein aggregates contain amyloid  
63 fibrils. Elucidating the structural nature of this novel type of protein instability would help to understand

64 the causes and consequences of protein aggregation during aging and to explain potential interactions  
65 with disease-aggregating proteins.

66 Since the initial discovery in *C. elegans*, age-dependent protein aggregation has been demonstrated in  
67 different organs in mammals (Ayyadevara, Balasubramaniam, et al., 2016; Ayyadevara, Mercanti, et al.,  
68 2016; Groh, Buhler, et al., 2017; Leeman et al., 2018; Tanase et al., 2016). Importantly, age-dependent  
69 protein aggregation is likely to be relevant in neurodegenerative processes. Indeed, the over-  
70 representation of proteins prone to aggregate with age among proteins sequestered in Alzheimer's  
71 disease inclusions of amyloid plaques and tau neurofibrillary tangles highlights a possible contribution to  
72 pathological processes (Ciryam, Tartaglia, Morimoto, Dobson, & Vendruscolo, 2013; David et al., 2010).  
73 Moreover, recent evidence shows that aggregates from wild-type aged mouse brains are a potent  
74 heterologous seed for amyloid- $\beta$  (A $\beta$ ) aggregation (Groh, Buhler, et al., 2017). However, because of the  
75 difficulties to distinguish the effects of protein aggregation from other consequences of aging, it is still  
76 not clear whether age-dependent protein aggregation plays a role in accelerating the aging process  
77 (David, 2012). A previous study has shown that *C. elegans* treated with RNAi targeting genes encoding  
78 aggregation-prone proteins tend to live longer than randomly chosen targets (Reis-Rodrigues et al.,  
79 2012). However, the interpretation of these results is complicated by the loss-of-function of these  
80 proteins. Recently, we found that aged animals with high aggregation levels of an RNA-binding protein  
81 (RBP) with a low-complexity prion-like domain were shorter lived, significantly smaller and less motile  
82 than animals with low RBP aggregation levels (Lechler et al., 2017). Still this evidence does not provide a  
83 definite answer to whether age-dependent protein aggregation plays a causal role in aging rather than  
84 being a simple by-product. To understand whether protein aggregation is protective or harmful, it is  
85 informative to look at how long-lived animals modulate protein solubility. Longevity mechanisms and  
86 enhanced proteostasis are tightly coupled (Taylor & Dillin, 2011). However, whereas several studies  
87 show reduced age-dependent protein aggregation in long-lived animals (David et al., 2010; Demontis &

88 Perrimon, 2010; Lechler et al., 2017), a recent study suggests that enhancing protein aggregation could  
89 be a strategy to promote longevity (Walther et al., 2015).

90 In the current study, we use a combination of transmission electron microscopy (TEM), fluorescence  
91 lifetime imaging (FLIM) (Kaminski Schierle et al., 2011), Thioflavin T (ThT) staining and structured  
92 illumination microscopy (SIM) (Young, Strohl, & Kaminski, 2016) to reveal amyloid-like structures in age-  
93 dependent protein aggregates *in vivo*. Unlike protein chemical instability caused by cumulative damage,  
94 age-dependent protein aggregates are formed by intrinsically aggregation-prone proteins, even shortly  
95 after their synthesis. We demonstrate that age-dependent protein aggregation is toxic and contributes  
96 to functional decline in *C. elegans*.

97

## 98 **Results:**

### 99 **Age-dependent aggregating proteins are intrinsically prone to aggregate in certain tissues.**

100 Previously, we performed an extensive characterization of the aggregation of two proteins, casein kinase  
101 I isoform alpha (KIN-19) and Ras-like GTP-binding protein rhoA (RHO-1). Both KIN-19 and RHO-1 were  
102 identified among the proteins with the highest propensity to become insoluble with age in wild-type *C.*  
103 *elegans* somatic tissues (David et al., 2010). *In vivo* analysis of animals expressing these proteins fused to  
104 fluorescent tags showed the appearance of immobile deposits with age (David et al., 2010). Among the  
105 insoluble proteome, the enrichment of certain physico-chemical features such as high aliphatic amino  
106 acid content or propensity to form  $\beta$ -sheet-rich structures shows that age-dependent protein  
107 aggregation is not random (David et al., 2010; Lechler et al., 2017; Walther et al., 2015). To understand  
108 whether KIN-19 and RHO-1 have an intrinsic capacity to aggregate similar to disease-associated proteins  
109 or whether a progressive accumulation of protein damage caused by non-enzymatic posttranslational  
110 modifications is required to induce their aggregation, we evaluated the dynamics of protein aggregation

111 *in vivo*. Protein labeling with mEOS2, a green-to-red photoconvertible fluorescent protein, has been  
112 successfully used to track protein dynamics (McKinney, Murphy, Hazelwood, Davidson, & Looger, 2009).  
113 In the present case, we used the mEOS2 tag to investigate how fast newly synthesized KIN-19 and RHO-1  
114 aggregate. For this purpose, we generated transgenic animals expressing KIN-19::mEOS2 in either the  
115 pharynx or in the body-wall muscles and transgenic animals expressing RHO-1::mEOS2 in the pharynx.  
116 The mEOS2 tag did not disrupt the aggregation potential of KIN-19, as the absence of fluorescence  
117 recovery after photobleaching confirms that both KIN-19::mEOS2 puncta in the pharynx and body-wall  
118 muscle are highly immobile structures (Figure supplement 1 A-D).

119 To follow newly synthesized proteins, we set-up a system to perform irreversible photoconversion of the  
120 mEOS2 tag present in live animals from green to red by exposing them to intense blue light. At a defined  
121 time-point, we photoconverted the mEOS present in aggregates to red. After the photoconversion,  
122 newly synthesized proteins emitted green fluorescence and could thus easily be distinguished from old  
123 (photoconverted/red) aggregates. This method allowed us to follow the rate of new aggregate formation  
124 and the rate of old aggregate removal in a population of transgenic animals over time. We observed  
125 photoconversion of all aggregates, but we also noted that the core region of some larger aggregates  
126 continued to emit green fluorescence (Figure 1 A, B). Interestingly, we observed a doubling in the  
127 number of animals with newly-formed green aggregates, 24 hours after the conversion at day 5 of  
128 adulthood in both the pharyngeal and body-wall muscles. Conversely, analysis of the red aggregates  
129 suggested a slow removal of old aggregates (Figure 1 A, B, Supplementary file 1). Blocking translation  
130 shortly before conversion reduced the formation of new aggregates (Figure 1 B). Conversion in young  
131 animals and blocking translation produced similar results (Figure supplement 1 E). Confocal imaging  
132 shows that newly synthesized KIN-19 associate with pre-existing aggregates (Figure 1 C). However, we  
133 also observed large aggregates emitting only green fluorescence suggesting that seeding is not a  
134 prerequisite for KIN-19 aggregate formation (Figure 1 C). We observed similar aggregation kinetics in

135 animals with RHO-1::mEOS2 expressed in the pharynx (Figure supplement 1 F). Together, these results  
136 reveal that aggregate formation can proceed rapidly after protein synthesis.

137

138 **Age-dependent protein aggregates contain amyloid-like structures *in vivo*.**

139 Both KIN-19 and RHO-1 are nearly identical to their human orthologues (sequence identity over 87%). X-  
140 ray diffraction shows that the human orthologues are globular proteins formed by a series of  $\alpha$ -helices  
141 and  $\beta$ -strands. The ability of KIN-19 and RHO-1 to aggregate shortly after synthesis suggests that their  
142 aggregation may be associated with the presence of folding intermediates. Notably, both proteins have  
143 several segments with a high amyloid propensity (Figure supplement 2 A, B) (Goldschmidt et al., 2010).  
144 This feature raises the possibility that KIN-19 and RHO-1 gain an amyloid-like conformation during their  
145 aggregation with age. We have previously shown that FLIM can be used to determine whether certain  
146 proteins are likely to form amyloid-like aggregates as the formation of amyloid fibrils leads to a  
147 significant drop in the fluorescence lifetime of the fluorescent-tagged amyloid proteins due to quenching  
148 (Chen et al., 2017; Kaminski Schierle et al., 2011; Murakami et al., 2015). In the current study, we applied  
149 FLIM to determine whether KIN-19 and RHO-1 form amyloid-like aggregates in live *C. elegans*. For this,  
150 we generated transgenic animals expressing translational fusions with the yellow fluorescent protein  
151 Venus in the pharynx. We first confirmed that there is an age-dependent increase in aggregate formation  
152 by KIN-19::Venus and RHO-1::Venus in the pharynx (Figure supplement 3 A, B) (Lechler et al., 2017).  
153 Using FLIM, we found that pharyngeal KIN-19 and RHO-1::Venus display a significantly decreased  
154 fluorescence lifetime compared to Venus only control worms (Figure 2 A-C, Figure supplement 4 A).  
155 Areas with the strongest drop in fluorescence lifetime co-localize with fluorescent-labeled aggregates  
156 (Figure 2 A). Of note, we also observed a similar drop in the fluorescence lifetime of pharyngeal RHO-1  
157 labeled with tagRFP compared to tagRFP alone (Figure supplementary 4 B). In both models with KIN-19  
158 and RHO-1, we observed a significant drop in the fluorescence lifetime already at day 1, consistent with

159 the appearance of aggregates in young animals due to protein overexpression. In particular, between  
160 day 1 and day 7 of adulthood, we measured a dramatic decrease in fluorescence lifetime of RHO-1  
161 aggregates and a more modest decrease in the fluorescence lifetime of KIN-19 aggregates. This result is  
162 consistent with the age-dependent increase in aggregate formation by both proteins and the fact that  
163 RHO-1 puncta tend to be larger and more solid than KIN-19 puncta. Indeed, all RHO-1 puncta evaluated  
164 showed no recovery after photobleaching whereas 30% of KIN-19 puncta showed some recovery as  
165 previously described (Figure supplement 3 C-E compared to (David et al., 2010)). In addition to  
166 evaluating the fluorescence lifetime, we assessed whether RHO-1 aggregates are stained by the Congo  
167 red derivative X34 previously used to detect amyloid deposits (Styren, Hamilton, Styren, & Klunk, 2000).  
168 Consistent with the amyloid-like nature of the aggregates, we observed co-localization of X34 with RHO-  
169 1 aggregates *in vivo* (Figure supplementary 4C-E).

170 To gain more insight into the capacity of RHO-1 to form amyloid-like fibrils, we expressed and purified  
171 recombinant RHO-1 (Figure supplement 5 A, B) and aggregated it over time by constant shaking in  
172 stabilizing buffer to induce fibrillisation at 37°C for a week. We obtained low quantities of RHO-1 fibrils,  
173 which we were able to analyze by TEM. Analysis of RHO-1 by TEM revealed fibril-like structures which  
174 resemble amyloid fibrils such as formed by huntingtin (Htt) (Figure supplement 5 C) (Reif, Chiki, Ricci, &  
175 Lashuel, 2018). Indeed, RHO-1 fibrils had a morphology more similar to Htt fibrils which are shorter and  
176 more branch-like compared to fibrils formed from other amyloids such as alpha-synuclein, which are  
177 long and flexible. Additionally, RHO-1 and Htt fibrils display no twisting which can be observed in alpha-  
178 synuclein fibrils, suggesting that the packing of the monomeric structure and the interaction between  
179 protofibrils may be different (Lyubchenko, Krasnoslobodtsev, & Luca, 2012). Importantly, already at day  
180 1, we found comparable fibrillary structures in extracts from RHO-1::Venus transgenic animals (Figure  
181 supplement 5 D). In order to confirm that similar fibril structures can be found in the absence of a  
182 fluorescent tag, we have isolated fibrils by affinity purification from day 7 old transgenic worms



183 expressing pharyngeal RHO-1::HisAvi and KIN-19::HisAvi and imaged them by TEM (Figure supplement  
184 5E). Moreover, we have stained isolated RHO-1::HisAvi day 7 fibrils, RHO-1::tagRFP day 2 fibrils and  
185 extracts from non-aggregated control worms day 2 with amyloid-binding molecule ThT. Using SIM, we  
186 found ThT positive RHO-1 fibrils as shown previously for polyglutamine and A $\beta$  fibrils in cells (Lu et al.,  
187 2019; Young et al., 2016) (Figure supplement 6).

188 Together, these findings strongly suggest that Casein kinase I isoform alpha and Ras-like GTP-binding  
189 protein rhoA aggregates contain amyloid-like structures *in vivo*.

190

### 191 **Age-dependent protein aggregation accelerates functional decline.**

192 A reliable indicator of human aging is a decline in physical capacity such as decreased muscle strength  
193 and coordination (Belsky et al., 2015). Similarly, *C. elegans* displays an age-related decline in pharyngeal  
194 pumping and body movement (Huang, Xiong, & Kornfeld, 2004). To investigate whether age-dependent  
195 protein aggregation accelerates functional decline with age, we measured pharyngeal pumping and  
196 swimming in liquid (thrashing) in transgenic animals overexpressing fluorescent-labeled KIN-19 and RHO-  
197 1 either in the pharynx or the body-wall muscles. In all models, protein aggregation increased with age,  
198 as measured by the change from a diffuse distribution to the formation of specific puncta by the  
199 fluorescent-tagged proteins (Figure supplement 7). Among the transgenic models generated, the largest  
200 age-dependent changes were observed for *C. elegans* expressing KIN-19::tagRFP in the pharynx (Figure  
201 supplement 7 A, E) (David et al., 2010). Whereas the majority of these transgenic animals have no  
202 aggregation at day 2, this dramatically changes with age and at day 8, the majority display high levels of  
203 KIN-19::tagRFP aggregation. Importantly, pumping frequency was strongly reduced in day 7 aged animals  
204 with the highest levels of pharyngeal KIN-19::tagRFP aggregation compared to those with the lowest  
205 aggregation levels (Figure 3 A, Supplementary file 2). The detrimental effect of age-dependent protein

206 aggregation was also apparent in animals with KIN-19::tagRFP aggregation in the body-wall muscles,  
207 since we observed an earlier decline in swimming frequency associated with KIN-19::tagRFP aggregation  
208 in the body-wall muscle (Figure supplement 8 A). This effect was amplified in animals with the highest  
209 level of aggregation (Figure 3 B). Of note, the fluorescent tagRFP expressed alone in the pharynx or in the  
210 body-wall muscle did not affect muscle function (Figure supplement 8 A, C). Decreased body movement  
211 with age is associated with increased sarcopenia characterized by disordered sarcomeres and reduced F-  
212 actin filaments (F-actin) (Baird et al., 2014; Herndon et al., 2002). To evaluate whether the presence of  
213 KIN-19 aggregates is linked to muscle damage at the cellular level, we assessed F-actin staining in animals  
214 with KIN-19 aggregation in the body-wall muscles. We found that animals with aggregates tended to  
215 have higher levels of disrupted sarcomeres compared to controls (Figure supplement 9 A, B).

216

217 To further show that protein aggregation is the cause of the functional decline in our transgenic animal  
218 models rather than other co-occurring aging factors, we examined the effects of protein aggregation in  
219 the absence of aging. Most likely due to the high level of overexpression in the pharyngeal muscles, RHO-  
220 1::tagRFP aggregated abundantly already in young animals (Figure supplement 7 C, E). We found that  
221 these high levels of RHO-1::tagRFP aggregation strongly impaired pharyngeal pumping in young animals  
222 (day 2) (Figure 3 C). Notably, these young animals displayed pumping rates normally observed only in  
223 aged animals. Moreover, RHO-1 aggregation disrupted actin filament structure in the pharyngeal  
224 muscles (Figure supplement 9C, D). To exclude that RHO-1 overexpression itself is toxic to *C. elegans*, we  
225 examined another transgenic model where RHO-1::Venus is expressed under the strong *C. elegans* body-  
226 wall muscle promoter *Punc-54*. These animals have similar levels of transgene expression compared to  
227 animals with body-wall muscle KIN-19::tagRFP (Figure supplement 7 F). Yet, whereas KIN-19 aggregates  
228 abundantly in the body-wall muscle, RHO-1::Venus hardly aggregates in this tissue (Figure supplement 7  
229 D). Thus, these transgenics are a suitable control to identify RHO-1 toxicity caused by overexpression.

230 Importantly, we did not observe reduced thrashing in animals with body-wall muscle RHO-1,  
231 demonstrating that overexpressed of RHO-1 without concomittant aggregation is not toxic (Figure 3 D).  
232 Similarly, the observation that only animals with the highest levels of pharyngeal KIN-19::tagRFP  
233 aggregation have functional impairment shows that KIN-19::tagRFP overexpression alone does not cause  
234 pumping defects (Figure 3 A and Figure supplement 8 B). Together, these positive and negative controls  
235 reveal that protein aggregation itself is detrimental in *C. elegans*.

236 Collectively, these findings show that animals with accelerated protein aggregation experience an earlier  
237 onset of functional decline in the tissues affected.

238

#### 239 **Discussion:**

240 Widespread protein aggregation in the context of normal aging has been observed in *C. elegans* (David et  
241 al., 2010; Reis-Rodrigues et al., 2012; Walther et al., 2015), *Drosophila* (Demontis & Perrimon, 2010),  
242 *Saccharomyces cerevisiae* (Peters et al., 2012) and in mammals, notably in neural stem cells (Leeman et  
243 al., 2018), heart (Ayyadevara, Mercanti, et al., 2016) and skeletal muscles (Ayyadevara,  
244 Balasubramaniam, et al., 2016), bone marrow and spleen (Tanase et al., 2016). Whereas these hundreds  
245 of proteins are maintained in a functional and soluble state in young animals, they lose their functional  
246 structure with age and accumulate into insoluble aggregates. The detergent insoluble properties and  
247 solid nature of the aggregates indicate similarities with disease-associated protein aggregation. However,  
248 until now it has not been known whether age-dependent protein aggregates display amyloid-like  
249 structures, a key characteristic of disease-associated protein aggregation. In this study, we focus on two  
250 normally globular proteins, Casein kinase I isoform alpha and Ras-like GTP-binding protein rhoA. We  
251 show that aggregates of either proteins display distinct fluorescence quenching properties characteristic  
252 of amyloid structures. In neurodegenerative diseases and amyloidosis, protein aggregation is a crucial

253 part of the pathological process. We demonstrate that aggregates formed by proteins prone to  
254 aggregation with age contribute to functional decline in the tissues affected. Our results predict that  
255 even if only a proportion of the hundreds of proteins becoming insoluble with age form harmful amyloid-  
256 like aggregates, this would be a significant cause of tissue aging for a variety of organs.

257 The speed of aggregate formation and the presence of amyloid-like structure brings significant insight  
258 into the aggregation process occurring during normal aging. We demonstrate that newly synthesized  
259 proteins rapidly assemble into large aggregates. The recruitment of newly synthesized proteins into  
260 existing aggregates indicates a seeding effect. However, we also observed the rapid formation of new  
261 aggregates entirely made up of newly synthesized proteins. This result shows that molecular aging of the  
262 protein caused by progressive accumulation of damage is not required for proteins to aggregate with  
263 age. Moreover, amyloid-like aggregates forming already in young animals indicate an intrinsic  
264 aggregation propensity. Therefore, it is likely that these proteins self-assemble into amyloid structures  
265 directly from unfolded or partially folded states occurring during or shortly after translation rather than  
266 undergoing unfolding from their natively folded state. This conclusion is consistent with the view that  
267 protein folding intermediates are particularly at risk of aggregating as exemplified by a recent study  
268 revealing that newly synthesized proteins constitute the majority of the insoluble fraction prompted by  
269 thermal stress (Xu et al., 2016). Furthermore, artificially increasing ribosome pausing during translation  
270 causes widespread protein aggregation (Nedialkova & Leidel, 2015). Both Casein kinase I isoform alpha  
271 and Ras-like GTP-binding protein rhoA contain several hexapeptides with high propensity for fibrillation  
272 which are normally buried in the fully folded protein (Figure supplement 2). Interestingly, the most  
273 prominent amyloid-promoting sequence for both proteins is localized near the N-terminus. Therefore,  
274 aberrant interactions may start already during translation. As protein aggregation typically results in loss  
275 of function, there is a strong evolutionary pressure to avoid this and molecular chaperones have evolved  
276 to recognize specifically sequences of high aggregation propensity (Rousseau, Serrano, & Schymkowitz,

277 2006). Our findings predict that age-dependent protein aggregation would result from decreased levels  
278 of molecular chaperones linked to protein synthesis rather than molecular chaperones induced by stress  
279 (Albanese, Yam, Baughman, Parnot, & Frydman, 2006; Pechmann, Willmund, & Frydman, 2013).  
280 Impaired proteasome-mediated removal of unfolded proteins directly after synthesis (Schubert et al.,  
281 2000) could also significantly contribute to age-dependent protein aggregation. Interestingly, the relative  
282 lack of Ras-like GTP-binding protein rhoA aggregation in the body-wall muscles compared to the  
283 pharyngeal muscles shows that this protein only aggregates within a specific cellular environment. Thus  
284 tissue-specific factors could be crucial for the aggregation process. These could be differences in the  
285 tissue proteostasis network and reliance on certain proteostasis components with age (Hamer,  
286 Matilainen, & Holmberg, 2010; Kern, Ackermann, Clement, Duerk, & Behl, 2010; Sala, Bott, & Morimoto,  
287 2017) but also age-related changes in the local tissue environment. For example, tissue-specific changes  
288 in ATP levels (Patel et al., 2017), availability of certain ions such as  $\text{Ca}^{2+}$  (Lautenschlager et al., 2018),  
289 redox state (Kirstein et al., 2015), could explain why certain proteins aggregate in one tissue but not  
290 another.

291 The resemblance between age-dependent protein aggregation and disease-associated protein  
292 aggregation raises the question whether they have similar proteotoxic mechanisms. Our results show  
293 that there is a strong correlation between the presence of large aggregates and impaired tissue function.  
294 In disease, intracellular aggregate toxicity is caused, at least in part, by sequestration and the resulting  
295 loss of function of essential cellular proteins (Hosp et al., 2017; Olzscha et al., 2011; Yu et al., 2014).  
296 Notably, proteostasis network components are significantly enriched in the age-dependent insoluble  
297 proteome (David et al., 2010). Therefore loss-of-function of proteins responsible for preventing  
298 aggregation could be a key source of toxicity. The correlation between large aggregates and  
299 proteotoxicity observed in the present study, does not exclude that intermediate forms on the path to  
300 age-dependent protein aggregation are also proteotoxic. Indeed, disease-associated pre-fibrillar species

301 or oligomers can be highly toxic by interacting through their hydrophobic side chains with other cellular  
302 components and in particular lipid membranes (Fusco et al., 2017; Knowles, Vendruscolo, & Dobson,  
303 2014; Walsh et al., 2002). Further experiments will be needed to characterize which types of  
304 intermediate species occur during age-dependent protein aggregation and to evaluate their potential  
305 toxicity. Conversely, it remains possible that some forms of age-dependent protein aggregation could be  
306 protective or manipulated to form harmless non-amyloid aggregates. Finally, it is possible that age-  
307 dependent protein aggregation occurring in one tissue will induce accelerated aging in another tissue.  
308 Following the evidence for seeding, self-propagation and cell-to-cell transfer of amyloid aggregating  
309 species in a disease context (Jucker & Walker, 2013), it is intriguing to speculate that the same  
310 mechanisms may arise with proteins aggregating during normal aging.

311 The proteotoxicity and amyloid conformation of age-dependent protein aggregation has important  
312 implications for diseases associated with protein aggregation. Accelerated functional decline and the  
313 overload of the proteostasis network caused by age-dependent protein aggregation could indirectly  
314 enhance disease-associated pathogenesis. There is also evidence for a direct connection between  
315 disease and aging-related aggregation. Indeed, a significant proportion of the proteins sequestered in  
316 disease pathological deposits are prone to aggregate with age (Ciryam et al., 2013; David et al., 2010).  
317 Notably, Casein kinase I isoform alpha is present in tau aggregates (Kannanayakal, Mendell, & Kuret,  
318 2008; Kuret et al., 1997). Therefore, age-dependent aggregation-prone proteins interact with disease-  
319 aggregating proteins in humans. Furthermore, we have demonstrated that minute amounts of insoluble  
320 proteins from aged wild-type mouse brains or aged *C. elegans* are sufficient to cross-seed amyloid- $\beta$   
321 aggregation *in vitro* (Groh, Buhler, et al., 2017). One possibility is that the highly hydrophobic nature of  
322 the amyloid-like structures in age-dependent protein aggregates provides a destabilizing surface that can  
323 promote the conformational conversion of disease-associated aggregating proteins. If the composition of  
324 the insoluble proteome is cell-specific, increases in age-dependent protein aggregation, for example

325 through higher expression or somatic aggregation-promoting mutations (Freer et al., 2016; Lodato et al.,  
 326 2018), could sensitize specific cells to disease-associated pathogenesis.

327 In summary, our study demonstrates that aggregation of proteins during normal aging resembles  
 328 pathological protein aggregation observed in neurodegenerative diseases and amyloidosis. We then  
 329 show that age-dependent protein aggregation causes early functional decline, a read-out of accelerated  
 330 aging. These findings emphasize age-dependent amyloid-like aggregation as an important target to  
 331 restore physical capacity and to promote healthy aging. Already promising results reveal that lysosome  
 332 activation in the germline and in aged neural stem cells clears protein aggregates and rejuvenates the  
 333 cells (Bohnert & Kenyon, 2017; Leeman et al., 2018).

334

335 **Methods:**

336 Key Resources Table :

Reagent type (species) or resource	Designation	Source or reference	Identifiers	Additional information
Gene ( <i>C. elegans</i> )	<i>kin-19</i>	Wormbase	WBGene00002202	
Gene ( <i>C. elegans</i> )	<i>rho-1</i>	Wormbase	WBGene00004357	
Strain ( <i>E. coli</i> )	OP50-1	Caenorhabditis genetic center (CGC)	<b>RRID:WB-STRAIN:OP50-1</b>	Streptomycin resistant strain of OP50
Genetic reagent ( <i>C. elegans</i> )	<i>muEx473[Pkin-19::kin-19::tagrfp + Ptp-1::gfp]</i>	doi: 10.1371/journal.pbio.1000450	<b>RRID:WB-STRAIN:CF3166</b>	N2 background
Genetic reagent ( <i>C. elegans</i> )	<i>muEx512[pkin-19::tagRFP + Ptp-1::GFP]</i>	doi: 10.1371/journal.pbio.1000450	CF3317	N2 background
Genetic reagent ( <i>C. elegans</i> )	<i>mulS209[Pmyo-3::kin-19::tagrfp + Ptp-1::gfp]</i>	doi: 10.1371/journal.pbio.1000450	CF3649	N2 background

Genetic reagent (C. elegans)	<i>muls210[pmyo-3::tagrfp + ptph-1::GFP]</i>	doi: 10.1371/journal.pbio.1000450	CF3650	N2 background
Genetic reagent (C. elegans)	<i>muEx587[Pkin-19::kin-19::meos2 + Punc-122::gfp]</i>	this paper	CF3706	N2 background
Genetic reagent (C. elegans)	<i>uqls9[Pmyo-2::rho-1::tagrfp + Ptp-1::gfp]</i>	this paper	DCD13	N2 background
Genetic reagent (C. elegans)	<i>uqEx4[Pmyo-3::kin-19::meos2]</i>	this paper	DCD69	N2 background
Genetic reagent (C. elegans)	<i>uqEx[Pmyo-2::rho-1::meos2 + Punc-122::gfp + cb-unc-119(+)]</i>	this paper	DCD83	injected into EG6699 containing ttTi5605II; unc-119(ed3)III
Genetic reagent (C. elegans)	<i>uqEx22[Punc-54::rho-1::venus]</i>	this paper	DCD127	N2 background
Genetic reagent (C. elegans)	<i>uqls12[Pmyo-2::rho-1::venus]</i>	this paper	DCD146	N2 background
Genetic reagent (C. elegans)	<i>uqEx37[Pkin-19::kin-19::venus + punc-122::gfp]</i>	doi: 10.1016/j.celrep.2016.12.033	DCD179	N2 background
Genetic reagent (C. elegans)	<i>uqls22 [pkin19::kin19::hisavi + pkin19::birAtagrfp]</i>	this paper	DCD242	fem-1(hc17ts)IV background
Genetic reagent (C. elegans)	<i>uqls19 [pmyo2::rho1::hisavi + pmyo2::birAtagrfp]</i>	this paper	DCD243	fem-1(hc17ts)IV background
Genetic reagent (C. elegans)	<i>uqEx49[pkin-19::meos]</i>	this paper	DCD245	N2 background
Genetic reagent (C. elegans)	<i>uqEx51[pmyo-2::venus]</i>	this paper	DCD248	N2 background
Genetic reagent (C. elegans)	<i>rmls126[Punc-54::YFP]</i>	<a href="https://doi.org/10.1073/pnas.152161099">https://doi.org/10.1073/pnas.152161099</a>	<b>RRID:WB-STRAIN:AM134</b>	N2 background
Genetic reagent (C. elegans)	<i>fem-1(hc17ts)IV</i>	CGC	<b>WB Cat# BA17, RRID:WB-STRAIN:BA17</b>	
recombinant DNA reagent	tagRFP	Evrogen, <a href="#">pTagRFP-N</a> , FP142		
recombinant DNA reagent	pKA1062 containing mEOS2	other		Kaveh Ashrafi, UCSF, USA
antibody	Phalloidin-iFluor™ 488 conjugate	ABD-23115, AAT Bioquest, Biomol, Germany		"1:50"



chemical compound, drug	X34	SML1954, Sigma-Aldrich, Germany		1mM final
chemical compound, drug	thioflavin T	#ab120751, abcam, UK		50 $\mu$ M
commercial assay or kit	5-Hydroxytryptamine creatinine sulfate complex	H7752, Sigma-Aldrich, Germany		10 $\mu$ M
commercial assay or kit	Nickel Sepharose 6 Fast Flow beads from HisTrap FF Crude column	GE Healthcare, Uppsala, Sweden		

337

338 Cloning and Strain Generation:

339 Cloning was carried out using the Gateway system (Life Technologies, Darmstadt, Germany). Pmyo-2  
340 promoter and pKA1062 mEOS2 translational vector were kindly provided by Dr. Brian Lee and Dr. Kaveh  
341 Ashrafi, UCSF. *rho-1* cDNA was amplified from a cDNA library prepared from total RNA isolated from N2  
342 worms. Plasmid containing biotinylation enzyme birA was kindly provided by Dr. Ekkehard Schulze  
343 (University Freiburg). All constructs contain the *unc-54* 3' UTR. The *tagrfp* vector was obtained from  
344 Evrogen (AXXORA, San Diego, CA, USA). Venus was generated by targeted mutation of the *yfp* gene.  
345 HisAvi tagged KIN-19 and RHO-1 were generated by cloning at the C-terminus a RGS6 tag together with  
346 a bacterially derived polypeptide serving as a biotinylation signal *in vivo* as previously described (Schaffer  
347 et al., 2010; Tagwerker et al., 2006). Constructs were sequenced at each step. Transgenics were  
348 generated by microinjection of the constructs at concentrations between 10 to 50 ng/ $\mu$ l into N2 animals.  
349 Stable lines were generated by irradiating the animals containing the extrachromosomal array in a CL-  
350 1000 Ultraviolet Crosslinker (UVP) with 275 $\mu$ J x 100. 100% transmission lines was backcrossed at least  
351 four times into the wild-type N2 strain.

352

353 Maintenance:

354 All strains were kept at 15°C on NGM plates inoculated with OP50 using standard techniques. Age-  
355 synchronization was achieved by transferring adults of the desired strain to 20°C and selecting their  
356 progeny at L4 stage. All experiments were performed at 20°C. Day 1 of adulthood starts 24h after L4.

357  
358 Photoconversion of mEOS2-tag and quantification of fluorescence levels:  
359 For photoconversion, worms were transferred onto a small (diameter 35 mm) NGM plate without food.  
360 The plate was placed 0.5 cm below a collimator (Collimator High-End Lumencor, Leica, Germany) fitted  
361 with a filter for blue fluorescence (387/11 BrightLine HC, diameter 40mm) and illuminated by a  
362 Lumencor Sola SE II (AHF, Tübingen). Conversion of mEOS2 in transgenic animals was performed four  
363 times for five minutes, with 2 minutes pauses between exposures. To reduce translation, worms were  
364 placed two hours before conversion on bacterial seeded plates with 500 µg/ml cycloheximide and kept  
365 after conversion on plates with cycloheximide for 48h during aggregation quantification.

366  
367 Aggregation quantification *in vivo*:  
368 Aggregation levels were determined using Leica fluorescence microscope M165 FC with a Planapo 2.0x  
369 objective. Aggregation was quantified following pre-set criteria adapted to the transgene expression  
370 pattern and levels in the different transgenic *C. elegans* models: Animals expressing *Pkin-19::KIN-*  
371 *19::mEOS2*, *Pkin-19::KIN-19::Venus* or *Pkin-19::KIN-19::TagRFP* were divided into less than 10 puncta  
372 (low aggregation), between 10 and 100 puncta (medium aggregation) and over 100 puncta in the  
373 anterior pharyngeal bulb (high aggregation). Animals overexpressing *Pmyo-2::RHO-1::Venus* were  
374 divided into less than 10 puncta in anterior or posterior pharyngeal bulb (low aggregation), over 10  
375 puncta in either bulbs (medium aggregation) and over 10 puncta in both bulbs (high aggregation).  
376 Because of extensive RHO-1 aggregation in animals overexpressing *Pmyo-2::RHO-1::TagRFP*, aggregation  
377 was only quantified in the isthmus: animals with no aggregation (low aggregation), animals with

378 aggregation in up to 50% (medium aggregation) and animals with aggregation in more than 50% (high  
379 aggregation) of the isthmus. Animals overexpressing *Pmyo-3::KIN-19::TagRFP* were divided into over 15  
380 puncta in the head or the middle body region (low aggregation), over 15 puncta in the head and the  
381 middle body region (medium aggregation) and over 15 puncta in head, middle body and tail region (high  
382 aggregation). The same categories defined for animals overexpressing *Pmyo-3::KIN-19::TagRFP* were  
383 used to evaluate animals overexpressing *Pmyo-3::KIN-19::mEOS2* with a cutoff of 10 puncta instead of 15  
384 to account for slightly lower aggregation levels. Animals overexpressing *Punc-54::RHO-1::Venus* were  
385 divided into two categories: less than 15 puncta in the whole animal (low aggregation) and over 15  
386 puncta in the whole animal (medium aggregation). Counting was done in a blind fashion. Two-tailed  
387 Fisher's exact test using an online tool (<https://www.socscistatistics.com/tests/fisher/default2.aspx>) was  
388 performed for statistical analysis.

389

390 Confocal imaging:

391 For confocal analysis using a Leica SP8 confocal microscope with the HC PL APO CS2 63x / 1.30 NA  
392 glycerol objective, worms were mounted onto slides with 2% agarose pads using 2  $\mu$ M levamisole for  
393 anaesthesia. Worms were examined using the Leica HyD hybrid detector. The tag mEOS2 was detected  
394 using 506nm as excitation and an emission range from 508-525nm for green fluorescence and 571nm as  
395 excitation and an emission range from 573-602nm for red fluorescence. 3D reconstructions were  
396 performed using the Leica Application Suite (LAS X). For X34 imaging, X34 was excited with a 405nm laser  
397 and detected with an emission window between 470-520nm and RHO-1::tagRFP using 555nm as  
398 excitation and an emission range from 565nm-620nm. For muscle structure imaging, phalloidin was  
399 visualized by excitation at 488nm and with an emission window between 506-551nm and KIN-  
400 19::tagRFP, RHO-1::tagRFP and tagRFP were visualized by excitation at 555nm and with an emission  
401 window between 560-650nm.

402 FRAP analysis was performed as previously described (David et al., 2010) using the Leica SP8 confocal  
403 microscope PMT detector. Relative fluorescence intensity (RFI) was analysed as described previously  
404 following the equation  $RFI = (Tt/Ct)/(T0/C0)$ , where T0 is the intensity in the region of interest (ROI)  
405 before photobleaching; Tt, the intensity in the ROI at a defined time after photobleaching; C0, the  
406 intensity in the non-bleached part of the puncta before photobleaching; and Ct, the intensity in the non-  
407 bleached part of the puncta after bleaching (Brignull, Morley, Garcia, & Morimoto, 2006).

408

409 Fluorescence lifetime imaging *in vivo*:

410 For fluorescence lifetime imaging, transgenic *C. elegans* were mounted on microscope slides with 2.5%  
411 agarose pads using 25 mM NaN<sub>3</sub> as anaesthetic. All samples were assayed on a modified confocal-based  
412 platform (Olympus FV300-IX70) equipped with a 60x oil objective (PLAPON 60XOSC2 1.4NA, Olympus,  
413 Germany) and integrated with time-correlated single photon counting (TCSPC) FLIM implementation. A  
414 pulsed supercontinuum (WL-SC-400-15, Fianium Ltd., UK) at 40MHz repetition rate served as the  
415 excitation source. YFP was excited at 510nm using a tuneable filter (AOTFnC-400.650, Quanta Tech, New  
416 York, USA). The excitation light was filtered with FF03-510/20 and the fluorescence emission was filtered  
417 with FF01-542/27 (both bandpass filters from Semrock Inc., New York, USA) before reaching the  
418 photomultiplier tube (PMC-100, Becker & Hickl GmbH, Berlin, Germany). Photons were recorded by a  
419 SPC-830 (Becker and Hickl GmbH, Germany) module that permits sorting photons from each pixel into a  
420 histogram according to the photon arrival times. Photons were acquired for two minutes to make a  
421 single 256 X 256 FLIM image and photobleaching was verified to be negligible during this time. Photon  
422 count rates were always kept below 1% of the laser repetition rate to avoid pulse pileup. All raw FLIM  
423 images were fitted with a single exponential decay function using FLIMfit (Warren et al., 2013) and  
424 exported to MATLAB (Mathworks, Inc., Natick, Massachusetts, USA) to obtain an intensity weighted

425 lifetime average for each image. Statistical analysis was carried out using two-way ANOVA followed by  
426 Sidak's multiple comparisons test in Graphpad Prism software (La Jolla, California, USA).

427

428 X34 staining:

429 Worms were incubated in 1 mM X-34 in 10 mM Tris-HCl pH 8 for two hours, gently shaking at room  
430 temperature as previously described (Link et al., 2001). Worms were then transferred to bacteria seeded  
431 NGM plates to destain overnight before confocal imaging.

432

433 Pharyngeal pumping analysis:

434 Electrical activity of the pharyngeal pumping was measured using the NemaMetrix ScreenChip System  
435 (NemaMetrix, Eugene OR). To record the electrical activity of pharynx pumping, the NemaMetrix  
436 ScreenChip System (NemaMetrix, Eugene OR) was used. The entire setup is housed in a laboratory that  
437 maintained a temperature of approximately 21°. Baseline noise was typically between 5 and 25  $\mu$ V.

438 For each experiment, 50 worms were picked in 1.5 ml of M9 + 0.01% Triton and washed 3 times via low-  
439 speed centrifugation. Worms were resuspended in 1.5 ml M9 + 0.01% Triton + 10  $\mu$ M 5-  
440 Hydroxytryptamine creatinine sulfate complex (Serotonin creatinine sulfate monohydrate) (Sigma,  
441 H7752) and incubated for 20 minutes. The ScreenChip system was placed on a stereoscope and loaded  
442 with a fresh screen chip. The screen chip was then vacuum-filled with M9 + 0.01% Triton +10  $\mu$ M 5-  
443 Hydroxytryptamine creatinine sulfate complex and the NemAquire software initiated for baseline noise  
444 checking. The animals were loaded into the recording channel of the screen chip via vacuum. After  
445 loading each animal, we waited at least 30 seconds or until the pumping became regular before starting  
446 to record. Each animal was recorded for approximately 2 minutes regardless of whether pumping activity  
447 was observed or not. Between 20-40 animals were recorded for each condition.

448 The recordings were analysed by NemAnalysis v0.2 software using the “Brute Force” optimization  
449 method. The ideal settings were chosen automatically from all combinations of the bounds settings  
450 (Minimum SNR from 1.4 (low) to 2.0 (high), with a Step size of 0.1; Highpass Cutoff from 10 (low) to 20  
451 (high), with a Step size of 5) and applied to produce the analysis results. Data was exported into Excel for  
452 statistical analysis. The student’s t test was used for statistical analysis.

453

454 Thrashing analysis:

455 To quantify movement in terms of body-bends-per-second, movies of worms swimming in liquid were  
456 acquired with high frame rates (15 frames per second) using a high-resolution monochrome camera (JAI  
457 BM-500 GE, Stemmer imaging GmbH, Puchheim, Germany). For each condition, around 40 animals were  
458 filmed (see Supplementary figure 1 for exact numbers). Worms were picked from cultivation plate and  
459 allowed to swim in a small plastic petri dish filled with M9 + 0.01% Triton. Petri dish containing worms  
460 was placed on a transparent platform and illuminated from bottom up with a flat backlight (CCS TH-  
461 211/200-RD, Stemmer imaging GmbH, Puchheim, Germany) to achieve homogeneous, high contrast  
462 lighting. The entire setup is housed in a laboratory that maintained a temperature of approximately 21°.  
463 Movies were taken 10 minutes after placing the animals in the liquid. Five consecutive 30-second movies  
464 were made for each group of worms. The movies were then analysed using the ImageJ wrMTrck plugin  
465 (Nussbaum-Krammer, Neto, Brielmann, Pedersen, & Morimoto, 2015). The wrMTrck plugin tracked  
466 individual worms in the movies and counted the numbers of body-bends. The input values of  
467 wrMTrck\_Batch are detailed in Supplementary file 3. Mann-Whitney test was used for statistical analysis  
468 (GraphPad Prism 7).

469

470 Analysis of muscle structure:

471 To analyse the muscle structures in the presence of aggregates, worms were collected at day 4 (for body-  
472 wall muscle KIN-19::tagRFP strain CF3649 and tagRFP control strain CF3650) and at day 2 (for pharyngeal  
473 RHO-1::tagrfp strain DCD13 and tagRFP control strain CF3317) and fixed in 4% PFA for 10 minutes at  
474 room temperature (RT). Worms were stained with phalloidin to visualize F-actin following a modified  
475 protocol by Karady et al. (Karady et al., 2013). Briefly, worms were washed in phosphate buffered saline  
476 (PBS), incubated for 30 minutes in PBS with 2% Tween and reduced for 30 minutes in Tris-Triton  $\beta$ -  
477 mercaptoethanol solution (5%  $\beta$ -mercaptoethanol, 1% triton X-100, 130mM Tris pH 6.8). After washing  
478 with PBS, worms were stained with phalloidin (1:50 in PBS, 0.5% triton X-100; Phalloidin-iFluor™ 488  
479 conjugate from AAT Bioquest), washed and mounted on slides for confocal imaging.

480 Image analysis of muscle structure was performed in a blind fashion. The body-wall muscle structure was  
481 considered normal when the actin filaments are smooth and tightly arranged with no empty space  
482 between, modest defective when some of the filaments were slightly distorted or less densely packed.  
483 Finally, body-wall muscles were considered severe defective when the filaments appeared significantly  
484 thinner or highly wrinkled, or with large empty space between. The pharyngeal muscle structure was  
485 considered severely defective when the actin filament structure showed large holes.

486  
487 Plasmid generation for RHO-1 recombinant expression:  
488 *C. elegans* RHO-1 cDNA was cloned into pET32a expression vector using restriction sites BamHI and  
489 HindIII (NEB, UK). The open reading frame encoded the RHO-1 fusion protein comprising of a thioredoxin  
490 protein, 6xHis tag and the Tobacco etch virus (TEV) cleavage recognition site with the sequence  
491 ENLYFQA, where TEV cleaves between Q and A, which was also the N-terminal residue of the Rho-1  
492 protein sequence, followed by the RHO-1 protein. The plasmid was confirmed by DNA sequencing  
493 (Source Bioscience, Cambridge, UK).

495 Expression and Isolation of Recombinant RHO-1 from Inclusion Bodies:

496 Reagents were purchased from Sigma-Aldrich, UK unless stated. BL21 DE3 STAR™ *E. coli* (Thermo Fisher  
497 Scientific, USA) were transformed with pET32a:RHO-1. 3 L cultures of *E. coli* in Lysogeny Broth containing  
498 carbenicillin (100 ug/mL) were grown at 37°C at 250 rpm and induced for expression of the RHO-1 fusion  
499 protein with 1 mM isopropyl-β-thiogalactopyranoside (IPTG) for four hours. *E. coli* were pelleted by  
500 centrifuge at 8000 x g for 15 minutes before being washed by resuspension in PBS with 1% Triton X-110  
501 and 1 mM Tris(2-carboxyethyl)phosphine hydrochloride (TCEP) and centrifuged again. The pelleted *E. coli*  
502 were either stored at -20°C until further use or lysed straight away. The RHO-1 fusion protein forms in  
503 inclusion bodies. To release the inclusion bodies, the *E. coli* were resuspended in 20 mL of lysis buffer per  
504 1 L of culture (50 mM Tris, 500 mM NaCl, 5 mM MgCl<sub>2</sub>, 1 mM phenylmethylsulfonyl fluoride (PMSF),  
505 protease inhibitor tablets (cComplete™, Mini EDTA-free, Roche), 1% Triton X-110, 1 mM TCEP, pH 8 at  
506 4°C) and sonicated on ice using three rounds of 30 s on and 30 s off 70% sonication power. The  
507 suspension was centrifuged at 10,000 x g for 10 minutes at 4°C. The pellet containing RHO-1 inclusion  
508 bodies was resuspended in 30 mL per 1 L culture of wash buffer 1 (Lysis buffer + 2 M urea, pH 8 at 4°C).  
509 The inclusion bodies were sonicated for four rounds of 10 s on, 20 s off and centrifuged at 10,000 x g for  
510 10 minutes at 4°C, this wash was then repeated again. Wash number 3 and 4 used the same sonication  
511 and centrifuge parameters, but pellets were washed with wash buffer 2 (Lysis buffer, 2 M urea, 1 mM  
512 TCEP, without Triton-110 or protease inhibitors). The final pellet became paler and more chalk-like.  
513 These wash steps are important to lead to a purer final RHO-1 protein. The inclusion bodies were then  
514 solubilised in solubilising buffer using 10 mL per 1 L of culture for 1 hour using a magnetic stirrer (50 mM  
515 Tris, 500 mM NaCl, 5 mM MgCl<sub>2</sub>, 6 M guanidinium hydrochloride (GuHCl), 1 mM TCEP, (6 M Urea can  
516 also be used in place of GuHCl, but GuHCl gives a slightly higher final protein yield)). Insoluble material  
517 was removed by centrifuge at 16,000 x g for 10 minutes at room temperature (RT).

518



519 Purification of Recombinant RHO-1:

520 The RHO-1 fusion protein was purified using two linked-together 1 mL HisTrap Crude FF columns on an  
521 ÄKTA Pure (GE Healthcare, Sweden). The columns were equilibrated with solubilising buffer before 10 mL  
522 of protein was loaded onto the column by the sample pump. The columns were washed in wash buffer  
523 (50 mM Tris, 500 mM NaCl, 5 mM MgCl<sub>2</sub>, 6 M Urea, 20 mM imidazole) before being eluted against a  
524 linear gradient of elution buffer (50 mM Tris, 500 mM NaCl, 5 mM MgCl<sub>2</sub>, 6 M Urea, 500 mM imidazole)  
525 over 16 column volumes of a 1 x 1 mL column, i.e. 16 mL. Multiple purification runs were performed until  
526 all RHO-1 fusion protein was purified. Fractions from all runs containing the RHO-1 fusion protein were  
527 pooled and dialysed overnight in 2 L stabilising buffer modified from ((Healthcare; Nelson, Lee, &  
528 Fremont, 2014; Thomson, Olson, Jackson, & Schrader, 2012) (50 mM Tris, 250 mM NaCl, 100 mM  
529 arginine, 5 mM reduced glutathione, 0.5 mM oxidised glutathione, 5 mM MgCl<sub>2</sub>, 5 μM guanosine 5'-  
530 diphosphate (GDP) (Generon, UK) pH 7.2). The RHO-1 fusion protein was then concentrated to 1 mL per  
531 1 L culture using Spectra/Gel Absorbent (Spectrum Labs, USA) through a 10 kDa MWCO Slide-A-Lyzer™  
532 dialysis cassette (Thermo Fisher Scientific). The RHO-1 fusion protein was then incubated overnight with  
533 recombinant TEV protease to cleave the RHO-1 from the fusion tag in a 1:50 ratio of TEV to RHO-1  
534 fusion protein based on absorbance at 280 nm. Recombinant TEV was produced by Dr Marielle Wälti  
535 using methods from (Tropea, Cherry, & Waugh, 2009). The cleaved RHO-1 was separated from the fusion  
536 tag and TEV protein by purification using the two linked-together 1 mL HisTrap Crude FF columns on an  
537 ÄKTA Pure. The columns were equilibrated in stabilising buffer and 1 mL of the protein loaded onto the  
538 columns by injection. Cleaved RHO-1 was eluted in stabilisation buffer during the column wash. The  
539 fusion tag and the His-tagged TEV were retained on the column and eluted with 100% elution buffer over  
540 10 CV (stabilisation buffer with 500 mM imidazole). Protein concentration was monitored throughout  
541 purification using the extinction coefficient 0.862 M<sup>-1</sup> cm<sup>-1</sup> for the fusion protein, 0.849 M<sup>-1</sup> cm<sup>-1</sup> for the  
542 refolded fusion protein and 0.875 M<sup>-1</sup> cm<sup>-1</sup> for the cleaved refolded RHO-1 protein. Quantitative analysis

543 of protein purity was performed in FIJI image analysis software (Schindelin et al., 2012) by profiling  
544 protein band intensity of the stained gel mass spectrometry confirmed the purification of RHO-1. To  
545 note, RHO-1 precipitated in NaP, Tris, NaCl buffers. RHO-1 protein mass was confirmed by mass  
546 spectrometry.

547

548 Fibrillisation of RHO-1 and analysis by Transmission Electron Microscopy (TEM):

549 RHO-1 was fibrillised by incubating 20  $\mu$ M in stabilising buffer during a Thioflavin-T (ThT) based-assay  
550 with 10  $\mu$ M ThT (AbCam, UK) in non-binding, clear bottom, black 96-well plate (PN 655906 Greiner Bio-  
551 One GmbH, Germany). The plate was incubated at 37°C with constant shaking at 300 rpm for 7 days.  
552 RHO-1 was taken from the wells in the microplate for imaging by TEM. All samples also contained 0.05%  
553  $\text{NaN}_3$  to prevent bacterial growth. Samples were incubated in an oven rotating at maximum speed (UVP  
554 HB-1000 Hybridizer, Fisher Scientific) at 37°C for five weeks.

555 Fibrillised RHO-1 samples were centrifuged for 20 minutes at 21,000 x g and the supernatant removed  
556 leaving 10  $\mu$ L of sample. Each 10  $\mu$ L sample was incubated on a glow-discharged copper grid for 1  
557 minute. Excess liquid was blotted off and the grid washed in twice in dH<sub>2</sub>O for 15 seconds. 2% uranyl  
558 acetate was used to negatively stain the samples for 30 s before imaging on the Tecnai G2 80-200kv TEM  
559 at the Cambridge Advanced Imaging Centre.

560

561 Preparation and analysis of worm lysates for fibrils by TEM:

562 *C. elegans* DCD146 expressing RHO-1::Venus, DCD242 expressing KIN-19::HisAvi and DCD243 expressing  
563 RHO-1::HisAvi were grown to confluency on high growth medium plates and bleached to obtain a  
564 synchronized population of worms as previously described (Sulston, 1988). L1s were transferred into a

565 liquid culture with complete S basal supplemented with OP50-1 (OP50 with Streptomycin resistance) and  
566 grown at 20°C or 25°C (to induce sterility of DCD242 and DCD243) as previously described (Groh, Buhler,  
567 et al., 2017; Groh, Gallotta, et al., 2017). At day 1 of adulthood (DCD146) or at day 7 of adulthood  
568 (DCD242 and DCD243), worms were allowed to sediment in a separation funnel and washed with cold  
569 M9. The worm pellet was resuspended in PBS with 2x protease inhibitor tablets (cOmplete™, Mini EDTA-  
570 free, Roche) and frozen in liquid nitrogen. For TEM with RHO-1::Venus, frozen worms were resuspended  
571 in radioimmunoprecipitation assay (RIPA) buffer with protease inhibitor tablets and lysed by 20-25  
572 passages through a cell homogeniser (Isobiotec, Germany) using a tungsten carbide ball with 16 µm  
573 clearance. Cuticle fragments and unlysed worms were removed by centrifugation for 5 min at 835 g and  
574 4 °C. After careful removal of the supernatant, the insoluble fraction was collected by centrifugation for  
575 30 min at 21,000 g and 4 °C. The supernatant was removed and the pellet was resuspended in PBS with  
576 protease inhibitor tablets by homogenising with a needle (27G, Sterican). To perform TEM with fibrils  
577 isolated by affinity, we pulled down His-tagged RHO-1 and KIN-19 by nickel beads. For this, 250 µL worm  
578 extract was added to 250 µL RIPA buffer (Invitrogen) with protease inhibitors and sonicated for 10s  
579 twice. Cuticle fragments and unlysed worms were removed by centrifugation for 1 minute at 800 x g. The  
580 supernatant was removed and centrifuged at 21 k x g for 20 minutes. The pellet was resuspended in 250  
581 µL PBS with protease inhibitors and passed through a 30 G needle three times. 20 µL of precharged  
582 Nickel Sepharose 6 Fast Flow beads taken from a HisTrap FF Crude column (GE Healthcare, Uppsala,  
583 Sweden) were incubated with the resuspended pellet overnight at 4°C on a fixed speed rotator at 20 rpm  
584 (SB2, Stuart, Staffordshire, UK). To separate the beads from unbound proteins the tubes were  
585 centrifuged at 800 x g for 1 min and the supernatant removed. 60 µL of 500 mM imidazole in PBS pH 8  
586 was added to the beads and incubated overnight at 4°C on a fixed speed rotator at 20 rpm. To isolate  
587 eluted fibrils the tubes were centrifuged at 800 x g for 1 min and the supernatant containing the fibrils  
588 was used for TEM experiments. 10 µL sample was applied to a carbon coated grid, and 2% uranyl acetate

589 was used for negative staining. Imaging was performed on the Tecnai G2 80-200kv TEM at the  
590 Cambridge Advanced Imaging Centre.

591  
592 Preparation and analysis of worm lysates for fibrils by SIM:  
593 Nunc® Lab-Tek® II Chamber Slide™ (Sigma, Dorset, UK) were coated for 30 min with 0.01 % poly-L-Lysine  
594 (P4707, Sigma) before incubation for one hour with either nickel bead extracted fibrils or resuspended  
595 worm pellets prepared as described above. RHO-1::tagRFP expressing transgenics (DCD13) and *fem-1(-)*  
596 mutants (CF2137; the non-aggregated control worm) extracts were incubated with 50 µM thioflavin T  
597 (ThT) (#ab120751, abcam, UK) for one hour and washed three times in PBS before imaging. To visualize  
598 amyloids from worm extracts, we used our custom-built SIM providing a spatial resolution approaching  
599 90 nm at frame rates reaching 22 Hz (Young et al., 2016). Hardware control and image reconstruction  
600 were performed with software written in LabView and Matlab (Strohl & Kaminski, 2015). For  
601 visualization, ImageJ was used.

602

603

604 **Acknowledgements:**

605 Some strains were provided by the CGC, which is funded by NIH Office of Research Infrastructure  
606 Programs (P40 OD010440). We thank Dr. Emily Crawford for generating the gateway vector with the  
607 histidine-avidin tag and Katja Widmaier for technical assistance.

608

609 **References:**

- 610 Albanese, V., Yam, A. Y., Baughman, J., Parnot, C., & Frydman, J. (2006). Systems analyses reveal two  
611 chaperone networks with distinct functions in eukaryotic cells. *Cell*, *124*(1), 75-88.  
612 doi:10.1016/j.cell.2005.11.039
- 613 Ayyadevara, S., Balasubramaniam, M., Suri, P., Mackintosh, S. G., Tackett, A. J., Sullivan, D. H., . . . Dennis,  
614 R. A. (2016). Proteins that accumulate with age in human skeletal-muscle aggregates contribute  
615 to declines in muscle mass and function in *Caenorhabditis elegans*. *Aging (Albany NY)*, *8*(12),  
616 3486-3497. doi:10.18632/aging.101141
- 617 Ayyadevara, S., Mercanti, F., Wang, X., Mackintosh, S. G., Tackett, A. J., Prayaga, S. V., . . . Mehta, J. L.  
618 (2016). Age- and Hypertension-Associated Protein Aggregates in Mouse Heart Have Similar  
619 Proteomic Profiles. *Hypertension*, *67*(5), 1006-1013. doi:10.1161/HYPERTENSIONAHA.115.06849
- 620 Baird, N. A., Douglas, P. M., Simic, M. S., Grant, A. R., Moresco, J. J., Wolff, S. C., . . . Dillin, A. (2014). HSF-  
621 1-mediated cytoskeletal integrity determines thermotolerance and life span. *Science*, *346*(6207),  
622 360-363. doi:10.1126/science.1253168
- 623 Belsky, D. W., Caspi, A., Houts, R., Cohen, H. J., Corcoran, D. L., Danese, A., . . . Moffitt, T. E. (2015).  
624 Quantification of biological aging in young adults. *Proc Natl Acad Sci U S A*, *112*(30), E4104-4110.  
625 doi:10.1073/pnas.1506264112
- 626 Bohnert, K. A., & Kenyon, C. (2017). A lysosomal switch triggers proteostasis renewal in the immortal *C.*  
627 *elegans* germ lineage. *Nature*, *551*(7682), 629-633. doi:10.1038/nature24620
- 628 Brignull, H. R., Morley, J. F., Garcia, S. M., & Morimoto, R. I. (2006). Modeling polyglutamine  
629 pathogenesis in *C. elegans*. *Methods Enzymol*, *412*, 256-282. doi:10.1016/S0076-6879(06)12016-  
630 9
- 631 Chen, W., Young, L. J., Lu, M., Zacccone, A., Strohl, F., Yu, N., . . . Kaminski, C. F. (2017). Fluorescence Self-  
632 Quenching from Reporter Dyes Informs on the Structural Properties of Amyloid Clusters Formed  
633 in Vitro and in Cells. *Nano Lett*, *17*(1), 143-149. doi:10.1021/acs.nanolett.6b03686
- 634 Chiti, F., Webster, P., Taddei, N., Clark, A., Stefani, M., Ramponi, G., & Dobson, C. M. (1999). Designing  
635 conditions for in vitro formation of amyloid protofilaments and fibrils. *Proc Natl Acad Sci U S A*,  
636 *96*(7), 3590-3594.
- 637 Ciryam, P., Tartaglia, G. G., Morimoto, R. I., Dobson, C. M., & Vendruscolo, M. (2013). Widespread  
638 aggregation and neurodegenerative diseases are associated with supersaturated proteins. *Cell*  
639 *Rep*, *5*(3), 781-790. doi:10.1016/j.celrep.2013.09.043
- 640 David, D. C. (2012). Aging and the aggregating proteome. *Front Genet*, *3*, 247.  
641 doi:10.3389/fgene.2012.00247
- 642 David, D. C., Ollikainen, N., Trinidad, J. C., Cary, M. P., Burlingame, A. L., & Kenyon, C. (2010). Widespread  
643 protein aggregation as an inherent part of aging in *C. elegans*. *PLoS Biol*, *8*(8), e1000450.  
644 doi:10.1371/journal.pbio.1000450
- 645 Demontis, F., & Perrimon, N. (2010). FOXO/4E-BP signaling in *Drosophila* muscles regulates organism-  
646 wide proteostasis during aging. *Cell*, *143*(5), 813-825. doi:10.1016/j.cell.2010.10.007
- 647 Finch, C. E., & Crimmins, E. M. (2016). Constant molecular aging rates vs. the exponential acceleration of  
648 mortality. *Proc Natl Acad Sci U S A*, *113*(5), 1121-1123. doi:10.1073/pnas.1524017113
- 649 Freer, R., Sormanni, P., Vecchi, G., Ciryam, P., Dobson, C. M., & Vendruscolo, M. (2016). A protein  
650 homeostasis signature in healthy brains recapitulates tissue vulnerability to Alzheimer's disease.  
651 *Sci Adv*, *2*(8), e1600947. doi:10.1126/sciadv.1600947
- 652 Fusco, G., Chen, S. W., Williamson, P. T. F., Cascella, R., Perni, M., Jarvis, J. A., . . . De Simone, A. (2017).  
653 Structural basis of membrane disruption and cellular toxicity by alpha-synuclein oligomers.  
654 *Science*, *358*(6369), 1440-1443. doi:10.1126/science.aan6160

655 Goldschmidt, L., Teng, P. K., Riek, R., & Eisenberg, D. (2010). Identifying the amyloids, proteins capable of  
656 forming amyloid-like fibrils. *Proc Natl Acad Sci U S A*, *107*(8), 3487-3492.  
657 doi:10.1073/pnas.0915166107

658 Golubev, A., Hanson, A. D., & Gladyshev, V. N. (2017). Non-enzymatic molecular damage as a prototypic  
659 driver of aging. *J Biol Chem*, *292*(15), 6029-6038. doi:10.1074/jbc.R116.751164

660 Gorisse, L., Pietrement, C., Vuiblet, V., Schmelzer, C. E., Kohler, M., Duca, L., . . . Gillery, P. (2016). Protein  
661 carbamylation is a hallmark of aging. *Proc Natl Acad Sci U S A*, *113*(5), 1191-1196.  
662 doi:10.1073/pnas.1517096113

663 Groh, N., Buhler, A., Huang, C., Li, K. W., van Nierop, P., Smit, A. B., . . . David, D. C. (2017). Age-  
664 Dependent Protein Aggregation Initiates Amyloid-beta Aggregation. *Front Aging Neurosci*, *9*,  
665 138. doi:10.3389/fnagi.2017.00138

666 Groh, N., Gallotta, I., Lechler, M. C., Huang, C., Jung, R., & David, D. C. (2017). Methods to Study Changes  
667 in Inherent Protein Aggregation with Age in *Caenorhabditis elegans*. *J Vis Exp*(129).  
668 doi:10.3791/56464

669 Hamer, G., Matilainen, O., & Holmberg, C. I. (2010). A photoconvertible reporter of the ubiquitin-  
670 proteasome system in vivo. *Nat Methods*, *7*(6), 473-478. doi:10.1038/nmeth.1460

671 Healthcare, G. E. Purifying Challenging Proteins Principles and Methods. *GE Healthcare*  
672 *Handbook*(Handbook 28-9095-31 AA).

673 Hekimi, S., Lapointe, J., & Wen, Y. (2011). Taking a "good" look at free radicals in the aging process.  
674 *Trends Cell Biol*, *21*(10), 569-576. doi:10.1016/j.tcb.2011.06.008

675 Herndon, L. A., Schmeissner, P. J., Dudaronek, J. M., Brown, P. A., Listner, K. M., Sakano, Y., . . . Driscoll,  
676 M. (2002). Stochastic and genetic factors influence tissue-specific decline in ageing *C. elegans*.  
677 *Nature*, *419*(6909), 808-814. doi:10.1038/nature01135

678 Hosp, F., Gutierrez-Angel, S., Schaefer, M. H., Cox, J., Meissner, F., Hipp, M. S., . . . Mann, M. (2017).  
679 Spatiotemporal Proteomic Profiling of Huntington's Disease Inclusions Reveals Widespread Loss  
680 of Protein Function. *Cell Rep*, *21*(8), 2291-2303. doi:10.1016/j.celrep.2017.10.097

681 Huang, C., Xiong, C., & Kornfeld, K. (2004). Measurements of age-related changes of physiological  
682 processes that predict lifespan of *Caenorhabditis elegans*. *Proc Natl Acad Sci U S A*, *101*(21),  
683 8084-8089. doi:10.1073/pnas.0400848101

684 Jucker, M., & Walker, L. C. (2013). Self-propagation of pathogenic protein aggregates in  
685 neurodegenerative diseases. *Nature*, *501*(7465), 45-51. doi:10.1038/nature12481

686 Kaeberlein, M. (2013). Longevity and aging. *F1000Prime Rep*, *5*, 5. doi:10.12703/P5-5

687 Kaminski Schierle, G. S., Bertocini, C. W., Chan, F. T. S., van der Goot, A. T., Schwedler, S., Skepper, J., . . .  
688 Kaminski, C. F. (2011). A FRET sensor for non-invasive imaging of amyloid formation in vivo.  
689 *Chemphyschem*, *12*(3), 673-680. doi:10.1002/cphc.201000996

690 Kannanayakal, T. J., Mendell, J. R., & Kuret, J. (2008). Casein kinase 1 alpha associates with the tau-  
691 bearing lesions of inclusion body myositis. *Neurosci Lett*, *431*(2), 141-145.  
692 doi:10.1016/j.neulet.2007.11.066

693 Karady, I., Frumkin, A., Dror, S., Shemesh, N., Shai, N., & Ben-Zvi, A. (2013). Using *Caenorhabditis elegans*  
694 as a model system to study protein homeostasis in a multicellular organism. *J Vis Exp*(82),  
695 e50840. doi:10.3791/50840

696 Kern, A., Ackermann, B., Clement, A. M., Duerk, H., & Behl, C. (2010). HSF1-controlled and age-associated  
697 chaperone capacity in neurons and muscle cells of *C. elegans*. *PLoS One*, *5*(1), e8568.  
698 doi:10.1371/journal.pone.0008568

699 Kirstein, J., Morito, D., Kakihana, T., Sugihara, M., Minnen, A., Hipp, M. S., . . . Morimoto, R. I. (2015).  
700 Proteotoxic stress and ageing triggers the loss of redox homeostasis across cellular  
701 compartments. *EMBO J*, *34*(18), 2334-2349. doi:10.15252/embj.201591711

702 Knowles, T. P., Vendruscolo, M., & Dobson, C. M. (2014). The amyloid state and its association with  
703 protein misfolding diseases. *Nat Rev Mol Cell Biol*, *15*(6), 384-396. doi:10.1038/nrm3810

704 Kuret, J., Johnson, G. S., Cha, D., Christenson, E. R., DeMaggio, A. J., & Hoekstra, M. F. (1997). Casein  
705 kinase 1 is tightly associated with paired-helical filaments isolated from Alzheimer's disease  
706 brain. *J Neurochem*, *69*(6), 2506-2515.

707 Lautenschlager, J., Stephens, A. D., Fusco, G., Strohl, F., Curry, N., Zacharopoulou, M., . . . Schierle, G. S. K.  
708 (2018). C-terminal calcium binding of alpha-synuclein modulates synaptic vesicle interaction. *Nat*  
709 *Commun*, *9*(1), 712. doi:10.1038/s41467-018-03111-4

710 Lechler, M. C., Crawford, E. D., Groh, N., Widmaier, K., Jung, R., Kirstein, J., . . . David, D. C. (2017).  
711 Reduced Insulin/IGF-1 Signaling Restores the Dynamic Properties of Key Stress Granule Proteins  
712 during Aging. *Cell Rep*, *18*(2), 454-467. doi:10.1016/j.celrep.2016.12.033

713 Leeman, D. S., Hebestreit, K., Ruetz, T., Webb, A. E., McKay, A., Pollina, E. A., . . . Brunet, A. (2018).  
714 Lysosome activation clears aggregates and enhances quiescent neural stem cell activation during  
715 aging. *Science*, *359*(6381), 1277-1283. doi:10.1126/science.aag3048

716 Link, C. D., Johnson, C. J., Fonte, V., Paupard, M., Hall, D. H., Styren, S., . . . Klunk, W. E. (2001).  
717 Visualization of fibrillar amyloid deposits in living, transgenic *Caenorhabditis elegans* animals  
718 using the sensitive amyloid dye, X-34. *Neurobiol Aging*, *22*(2), 217-226.

719 Lodato, M. A., Rodin, R. E., Bohrsen, C. L., Coulter, M. E., Barton, A. R., Kwon, M., . . . Walsh, C. A. (2018).  
720 Aging and neurodegeneration are associated with increased mutations in single human neurons.  
721 *Science*, *359*(6375), 555-559. doi:10.1126/science.aao4426

722 Lu, M., Williamson, N., Mishra, A., Michel, C. H., Kaminski, C. F., Tunnaclyffe, A., & Kaminski Schierle, G. S.  
723 (2019). Structural progression of amyloid-beta Arctic mutant aggregation in cells revealed by  
724 multiparametric imaging. *J Biol Chem*, *294*(5), 1478-1487. doi:10.1074/jbc.RA118.004511

725 Lyubchenko, Y. L., Krasnoslobodtsev, A. V., & Luca, S. (2012). Fibrillogenesis of huntingtin and other  
726 glutamine containing proteins. *Subcell Biochem*, *65*, 225-251. doi:10.1007/978-94-007-5416-  
727 4\_10

728 McKinney, S. A., Murphy, C. S., Hazelwood, K. L., Davidson, M. W., & Looger, L. L. (2009). A bright and  
729 photostable photoconvertible fluorescent protein. *Nat Methods*, *6*(2), 131-133.  
730 doi:10.1038/nmeth.1296

731 Murakami, T., Qamar, S., Lin, J. Q., Schierle, G. S., Rees, E., Miyashita, A., . . . St George-Hyslop, P. (2015).  
732 ALS/FTD Mutation-Induced Phase Transition of FUS Liquid Droplets and Reversible Hydrogels  
733 into Irreversible Hydrogels Impairs RNP Granule Function. *Neuron*, *88*(4), 678-690.  
734 doi:10.1016/j.neuron.2015.10.030

735 Nedialkova, D. D., & Leidel, S. A. (2015). Optimization of Codon Translation Rates via tRNA Modifications  
736 Maintains Proteome Integrity. *Cell*, *161*(7), 1606-1618. doi:10.1016/j.cell.2015.05.022

737 Nelson, C. A., Lee, C. A., & Fremont, D. H. (2014). Oxidative refolding from inclusion bodies. *Methods Mol*  
738 *Biol*, *1140*, 145-157. doi:10.1007/978-1-4939-0354-2\_11

739 Nussbaum-Krammer, C. I., Neto, M. F., Brielmann, R. M., Pedersen, J. S., & Morimoto, R. I. (2015).  
740 Investigating the spreading and toxicity of prion-like proteins using the metazoan model  
741 organism *C. elegans*. *J Vis Exp*(95), 52321. doi:10.3791/52321

742 Olzscha, H., Schermann, S. M., Woerner, A. C., Pinkert, S., Hecht, M. H., Tartaglia, G. G., . . . Vabulas, R.  
743 M. (2011). Amyloid-like aggregates sequester numerous metastable proteins with essential  
744 cellular functions. *Cell*, *144*(1), 67-78. doi:10.1016/j.cell.2010.11.050

745 Patel, A., Malinowska, L., Saha, S., Wang, J., Alberti, S., Krishnan, Y., & Hyman, A. A. (2017). ATP as a  
746 biological hydrotrope. *Science*, *356*(6339), 753-756. doi:10.1126/science.aaf6846

747 Pechmann, S., Willmund, F., & Frydman, J. (2013). The ribosome as a hub for protein quality control. *Mol*  
748 *Cell*, *49*(3), 411-421. doi:10.1016/j.molcel.2013.01.020

749 Peters, T. W., Rardin, M. J., Czerwieniec, G., Evani, U. S., Reis-Rodrigues, P., Lithgow, G. J., . . . Hughes, R.  
750 E. (2012). Tor1 regulates protein solubility in *Saccharomyces cerevisiae*. *Mol Biol Cell*, *23*(24),  
751 4679-4688. doi:10.1091/mbc.E12-08-0620

752 Reif, A., Chiki, A., Ricci, J., & Lashuel, H. A. (2018). Generation of Native, Untagged Huntingtin Exon1  
753 Monomer and Fibrils Using a SUMO Fusion Strategy. *J Vis Exp*(136). doi:10.3791/57506  
754 Reis-Rodrigues, P., Czerwieniec, G., Peters, T. W., Evani, U. S., Alavez, S., Gaman, E. A., . . . Hughes, R. E.  
755 (2012). Proteomic analysis of age-dependent changes in protein solubility identifies genes that  
756 modulate lifespan. *Aging Cell*, *11*(1), 120-127. doi:10.1111/j.1474-9726.2011.00765.x  
757 Rousseau, F., Serrano, L., & Schymkowitz, J. W. (2006). How evolutionary pressure against protein  
758 aggregation shaped chaperone specificity. *J Mol Biol*, *355*(5), 1037-1047.  
759 doi:10.1016/j.jmb.2005.11.035  
760 Sala, A. J., Bott, L. C., & Morimoto, R. I. (2017). Shaping proteostasis at the cellular, tissue, and  
761 organismal level. *J Cell Biol*, *216*(5), 1231-1241. doi:10.1083/jcb.201612111  
762 Schaffer, U., Schlosser, A., Muller, K. M., Schafer, A., Katava, N., Baumeister, R., & Schulze, E. (2010).  
763 SnAvi--a new tandem tag for high-affinity protein-complex purification. *Nucleic Acids Res*, *38*(6),  
764 e91. doi:10.1093/nar/gkp1178  
765 Schindelin, J., Arganda-Carreras, I., Frise, E., Kaynig, V., Longair, M., Pietzsch, T., . . . Cardona, A. (2012).  
766 Fiji: an open-source platform for biological-image analysis. *Nat Methods*, *9*(7), 676-682.  
767 doi:10.1038/nmeth.2019  
768 Schubert, U., Anton, L. C., Gibbs, J., Norbury, C. C., Yewdell, J. W., & Bennink, J. R. (2000). Rapid  
769 degradation of a large fraction of newly synthesized proteins by proteasomes. *Nature*,  
770 *404*(6779), 770-774. doi:10.1038/35008096  
771 Strohl, F., & Kaminski, C. F. (2015). A joint Richardson-Lucy deconvolution algorithm for the  
772 reconstruction of multifocal structured illumination microscopy data. *Methods Appl Fluoresc*,  
773 *3*(1), 014002. doi:10.1088/2050-6120/3/1/014002  
774 Styren, S. D., Hamilton, R. L., Styren, G. C., & Klunk, W. E. (2000). X-34, a fluorescent derivative of Congo  
775 red: a novel histochemical stain for Alzheimer's disease pathology. *J Histochem Cytochem*, *48*(9),  
776 1223-1232. doi:10.1177/002215540004800906  
777 Sulston, J. H., J. . (1988). *The Nematode Caenorhabditis elegans* Cold Spring Harbor: Cold Spring Harbor  
778 Laboratory Press.  
779 Tagwerker, C., Flick, K., Cui, M., Guerrero, C., Dou, Y., Auer, B., . . . Kaiser, P. (2006). A tandem affinity tag  
780 for two-step purification under fully denaturing conditions: application in ubiquitin profiling and  
781 protein complex identification combined with in vivocross-linking. *Mol Cell Proteomics*, *5*(4), 737-  
782 748. doi:10.1074/mcp.M500368-MCP200  
783 Tanase, M., Urbanska, A. M., Zolla, V., Clement, C. C., Huang, L., Morozova, K., . . . Santambrogio, L.  
784 (2016). Role of Carbonyl Modifications on Aging-Associated Protein Aggregation. *Sci Rep*, *6*,  
785 19311. doi:10.1038/srep19311  
786 Taylor, R. C., & Dillin, A. (2011). Aging as an event of proteostasis collapse. *Cold Spring Harb Perspect*  
787 *Biol*, *3*(5). doi:10.1101/cshperspect.a004440  
788 Thomson, C. A., Olson, M., Jackson, L. M., & Schrader, J. W. (2012). A simplified method for the efficient  
789 refolding and purification of recombinant human GM-CSF. *PLoS One*, *7*(11), e49891.  
790 doi:10.1371/journal.pone.0049891  
791 Tropea, J. E., Cherry, S., & Waugh, D. S. (2009). Expression and purification of soluble His(6)-tagged TEV  
792 protease. *Methods Mol Biol*, *498*, 297-307. doi:10.1007/978-1-59745-196-3\_19  
793 Vermulst, M., Denney, A. S., Lang, M. J., Hung, C. W., Moore, S., Moseley, M. A., . . . Erie, D. A. (2015).  
794 Transcription errors induce proteotoxic stress and shorten cellular lifespan. *Nat Commun*, *6*,  
795 8065. doi:10.1038/ncomms9065  
796 Walsh, D. M., Klyubin, I., Fadeeva, J. V., Cullen, W. K., Anwyl, R., Wolfe, M. S., . . . Selkoe, D. J. (2002).  
797 Naturally secreted oligomers of amyloid beta protein potently inhibit hippocampal long-term  
798 potentiation in vivo. *Nature*, *416*(6880), 535-539. doi:10.1038/416535a



799 Walther, D. M., Kasturi, P., Zheng, M., Pinkert, S., Vecchi, G., Ciryam, P., . . . Hartl, F. U. (2015).  
800 Widespread Proteome Remodeling and Aggregation in Aging *C. elegans*. *Cell*, *161*(4), 919-932.  
801 doi:10.1016/j.cell.2015.03.032  
802 Warren, S. C., Margineanu, A., Alibhai, D., Kelly, D. J., Talbot, C., Alexandrov, Y., . . . French, P. M. (2013).  
803 Rapid global fitting of large fluorescence lifetime imaging microscopy datasets. *PLoS One*, *8*(8),  
804 e70687. doi:10.1371/journal.pone.0070687  
805 Xu, G., Pattamatta, A., Hildago, R., Pace, M. C., Brown, H., & Borchelt, D. R. (2016). Vulnerability of newly  
806 synthesized proteins to proteostasis stress. *J Cell Sci*, *129*(9), 1892-1901. doi:10.1242/jcs.176479  
807 Young, L. J., Strohl, F., & Kaminski, C. F. (2016). A Guide to Structured Illumination TIRF Microscopy at  
808 High Speed with Multiple Colors. *J Vis Exp*(111). doi:10.3791/53988  
809 Yu, A., Shibata, Y., Shah, B., Calamini, B., Lo, D. C., & Morimoto, R. I. (2014). Protein aggregation can  
810 inhibit clathrin-mediated endocytosis by chaperone competition. *Proc Natl Acad Sci U S A*,  
811 *111*(15), E1481-1490. doi:10.1073/pnas.1321811111

812

813

814 **Figure legends**

815 **Figure 1: Newly synthesized KIN-19 rapidly transitions into aggregates in aged animals**

816 (A, B) Following photoconversion at day 5 in the pharynx or in the body-wall muscle, the number of  
817 animals with newly synthesized green-emitting non-converted KIN-19::mEOS2 aggregates doubles over  
818 24 hours. Conversely levels of red-emitting converted aggregates slowly declines. Blocking translation  
819 with cycloheximide (CHX) prevents new aggregate formation (B). Aggregation is evaluated in *Pkin-*  
820 *19::KIN-19::mEOS2* and *Pmyo-3::KIN-19::mEOS2* transgenic animals on the basis of the fluorescence  
821 intensity in puncta, representing aggregation (see methods). Quantification was done in the same  
822 population of *C. elegans* before conversion (BC), after conversion (AC), 24h after conversion and 48h  
823 after conversion. Fisher's exact test comparing low versus medium + high aggregation levels to after  
824 conversion: \*p < 0.05, \*\*p < 0.01, \*\*\*\*p < 0.0001. Fisher's exact test comparing low + medium versus  
825 high aggregation levels to after conversion: °°p < 0.01. See source data including independent biological  
826 repeat in supplementary file 1.

827 (C) 24 hours after photoconversion at day 7, newly synthesized KIN-19::mEOS2 (green emitting) forms  
828 new aggregates and associates around older aggregates (red emitting). 3D reconstruction in the  
829 pharyngeal anterior bulb region. Arrow heads highlight large new aggregates formed independently of  
830 previous aggregates. Scale bar 2 µm.

831  
832 **Figure supplement 1 (related to Figure 1): Newly synthesized KIN-19 and RHO-1 rapidly transitions into**  
833 **aggregates in young animals**

834 (A) KIN-19::mEOS2 puncta visible in the body wall muscle contain immobile protein, demonstrated by  
835 lack of fluorescent recovery after photobleaching (FRAP) after 5 minutes. Area bleached enlarged in  
836 caption. Scale bar 2 µm.

837 (B) KIN-19::mEOS2 puncta visible in the pharynx contain immobile protein, demonstrated by FRAP after 8  
838 minutes. Area bleached enlarged in caption. Scale bar 2  $\mu$ m.

839 (C) FRAP analysis of KIN-19::mEOS2 puncta present in aged worms. Quantification of relative  
840 fluorescence intensity (RFI) over time. Number of animals = 4, puncta evaluated = 6, mean  $\pm$  SD is  
841 represented. See source data in supplementary file 1.

842 (D) FRAP analysis of mEOS2 puncta/areas of fluorescence present in aged worms. Number of animals = 3,  
843 puncta evaluated = 6, mean  $\pm$  SD is represented. Only a few puncta are present in a population of  
844 animals overexpressing *Pkin-19::mEOS2* (one in 80 transgenics at day 9 had more than 10 puncta in  
845 anterior bulb).

846 (E) In young animals, aggregates are formed by newly synthesized KIN-19 and inhibition of translation (by  
847 cycloheximide (CHX)) reduces new aggregate formation. Aggregation is evaluated in *Pkin-19::KIN-*  
848 *19::mEOS2* transgenic animals on the basis of the fluorescence intensity in puncta, representing  
849 aggregation (see methods). Quantification was done in the same population of *C. elegans* before  
850 conversion (BC) at day 2, after conversion (AC), 24h after conversion and 48h after conversion. Fisher's  
851 exact test comparing low versus medium + high aggregation levels to after conversion: \*p < 0.05, \*\*p <  
852 0.01, \*\*\*\*p < 0.0001. See source data in supplementary file 1.

853  
854 (F) RHO-1::mEOS2 aggregates strongly already at day 1 and forms new aggregates (green) 24 h after  
855 photoconversion and associates with older aggregates (red). Scale bar 15  $\mu$ m, 7  $\mu$ m in zoom.

856  
857 **Figure 2: Drop in fluorescence lifetime reveals amyloid-like structure of KIN-19 and RHO-1 aggregates**  
858 **in live *C. elegans*.**

859 (A) Representative intensity-weighted FLIM images of Venus only (control), RHO-1::Venus and KIN-  
860 19::Venus worms. Scale = 25  $\mu$ m. Inset shows zoomed-in images (intensity and FLIM) of the anterior bulb  
861 for Venus only, RHO-1::Venus and KIN-19::Venus worms at day 12. Scale = 25  $\mu$ m.

862 (B) Scatter plot shows a drop in the intensity-weighted fluorescence lifetime averages in adult worms  
863 expressing RHO-1::Venus and KIN-19::Venus compared to worms expressing Venus only (control) in the  
864 pharynx. n = 7-10, 2 independent biological repeats. Data is shown as mean lifetime +/- SEM and the  
865 statistical analysis was performed using two-way ANOVA with Sidak's multiple comparisons test: \*\*  
866 p<0.01, \*\*\*\* p<0.0001. See source data in supplementary file 1.

867 (C) Normalised histograms of intensity-weighted fluorescence lifetimes for RHO-1::Venus and KIN-  
868 19::Venus show a population shift towards lower lifetimes compared to Venus only (control) worms. The  
869 histograms contain information from all pixels of all images acquired for each condition.

870

871 **Figure supplement 2 (related to Figure 2): Fibrillation propensity calculate by ZipperDB**

872 (A) Fibrillation propensity profile for KIN-19

873 (B) Fibrillation propensity profile for RHO-1

874 Table inset shows hexapeptides with Composite scores below -45.

875 ZipperDB: <https://services.mbi.ucla.edu/zipperdb/>

876

877 **Figure supplement 3 (related to Figure 2): Aggregation with age of RHO-1::Venus and KIN-19::Venus**

878 (A) Increased pharyngeal KIN-19 aggregation with age in animals expressing *Pkin-19::KIN-19::Venus*.

879 Panel reproduced from <https://doi.org/10.1016/j.celrep.2016.12.033>.

880 (B) Increased pharyngeal RHO-1 aggregation with age in animals expressing *Pmyo-2::RHO-1::Venus*.

881 Numbers of worms indicated in the bars. Significance calculated low + medium versus high aggregation  
882 levels compared to day 2 of adulthood; Fisher's exact test: \*\*\*\*p< 0.0001. See source data in  
883 supplementary file 1.

884 (C) RHO-1::Venus puncta visible in the pharynx contain immobile protein, demonstrated by absence of  
885 fluorescence recovery after 4 minutes. Scale bar 2  $\mu$ m.

886 (D) RHO-1::Venus aggregates are highly immobile. Table summarizes FRAP experiments carried out at  
887 different ages.

888 (E) FRAP analysis of RHO-1::Venus puncta present in aged worms compared to Venus alone.  
889 Quantification of RFI over time. Number of animals = 5, puncta evaluated = 6, mean  $\pm$  SD is represented.  
890 See source data in supplementary file 1.

891

892 **Figure supplement 4 (related to Figure 2): Staining of RHO-1::tagRFP with Congo red derivative X34**

893 (A) Representative fluorescence decay curves, lifetime fits (with associated  $\chi^2$  values) and fit residuals  
894 for Venus only (control), RHO-1::Venus and KIN-19::Venus adult worms at day 12. The black trace  
895 represents the instrument response function (IRF).

896 (B) Drop in fluorescence lifetime upon RHO-1::tagRFP aggregation. Scatter plot showing the intensity-  
897 weighted mean fluorescence lifetime values of day 1 adult worms expressing RHO-1::tagRFP in the  
898 pharynx compared to worms expressing tagRFP only. n = 7-8, 2 independent biological repeats  
899 combined. t-test with Welch's correction for unequal standard deviations: \*\*\*\* p<0.0001.

900 See source data in supplementary file 1.

901 (C) RHO-1 aggregates are stained by Congo red derivative X34. Day 2 old animals expressing *Pmyo-*  
902 *2::RHO-1::tagRFP*. Scale bar 30  $\mu$ m. Zoom scale bar 15  $\mu$ m.

903 (D) Absence of X34 staining in wild-type pharynx. Day 3 old wild-type animals (N2). Scale bar 30  $\mu$ m.

904 Zoom scale bar 15  $\mu$ m.

905 (E) RHO-1::tagRFP fluorescence does not interfere with X34 fluorescence as demonstrated by eliminating

906 tagRFP fluorescence by bleaching (in white square). Scale bar 3  $\mu$ m.

907

908 **Figure supplement 5 (related to Figure 2): Recombinant RHO-1 forms amyloid-like fibrils *in vitro* and *in***

909 ***vivo***

910 (A) Purification steps of recombinant RHO-1 analyzed by SDS-PAGE gel electrophoresis and Coomassie

911 staining. The RHO-1 fusion protein consisting of the thioredoxin protein, His tag and Tobacco etch virus

912 (TEV) cleavage recognition site was purified on a Crude FF column and eluted with imidazole. It ran

913 slightly quicker than the expected 40 kDa predicted size (lane 1). The fusion protein was incubated with

914 recombinant TEV protease overnight in a 1:50 ratio (lane 2). The cleaved RHO-1 protein did not bind to

915 the Crude FF column and eluted in the flow through (lane 3). The TEV protease which has a 6xHis tag and

916 the remaining uncleaved fusion protein were eluted from the column with imidazole (lane 4).

917 (B) Matrix Assisted Laser Desorption/Ionization (MADLI) mass spectrometry of purified RHO-1.

918 Performed by the Proteomics Facility, Biochemistry Department, University of Cambridge.

919 (C) Negative-stain transmission electron micrographs of fibrillised RHO-1. TEM of RHO-1 negatively

920 stained using 2% uranyl acetate. RHO-1 was incubated for 1 week in a ThT assay to fibrillise. Scale bar =

921 200 nm.

922 (D) Negative-stain transmission electron micrographs of *pmyo-2::RHO-1::Venus* worm lysates, day 1. TEM

923 of RHO-1 fibrils negatively stained using 2% uranyl acetate. Scale bar = 200 nm.

924 (E) Negative-stain transmission electron micrographs of RHO-1::HisAvi and KIN-19::HisAvi purified from  
925 worms lysates with nickel beads, day 7. Scale bar = 200 nm.

926  
927 **Figure supplement 6 (related to Figure 2): Structured illumination microscopy reveals that RHO-1**  
928 **forms ThT positive fibril structures *in vivo***

929 (A) Left image: SIM image of RHO-1 fibrils isolated by affinity purification from transgenics expressing  
930 RHO-1::HisAvi at day 7 and labelled using the amyloid dye ThT. Right image: Zoomed in image of left  
931 image highlighting the fibril bundles formed by RHO-1 *in vivo*. Circled in red, single fibrils; in green, fibril  
932 bundles and in blue, fibril clusters. Scale bars: 5 and 1  $\mu\text{m}$ , respectively. (B) Two colour SIM images of  
933 RHO-1 fibrils extracted from transgenics expressing RHO-1::tagRFP (day 2). Fibrils were stained with ThT  
934 prior to imaging. Left image: SIM image of ThT positive RHO-1::tagRFP fibrils. Central image: SIM image  
935 of the same fibril as shown in left but upon tagRFP excitation. Right image: Overlay of ThT and tagRFP  
936 channels displays co-localization of ThT and RFP of extracted RHO-1::tagRFP fibrils. Lower panel: imaging  
937 of control extracts from young animals (sterile *fem-1(-)* mutants). Scale bar: 1  $\mu\text{m}$ .

938  
939 **Figure 3: Age-dependent protein aggregation impairs pharyngeal and body-wall muscle function.**

940 (A) Aged animals with high levels of pharyngeal KIN-19 aggregation have reduced pharyngeal pumping.  
941 N= 23-28 animals analyzed per group. T-test:  $p < 0.0001$ .

942 (B) Aged animals with high levels of KIN-19 aggregation in the body-wall muscle display reduced  
943 thrashing. Mean body bends per seconds are set to 100% in animals with low aggregation. Mann-  
944 Whitney test:  $p < 0.0001$ .

945 (C) Young animals with RHO-1 aggregation in pharynx have impaired pharyngeal pumping. N= 26-27  
946 animals analyzed per group. T-test:  $p < 0.0001$ .

947 (D) Overexpression of RHO-1 without aggregation in the body-wall muscles does not influence thrashing.  
948 Mean body bends per seconds are set to 100% in *Punc-54::yfp* transgenic animals. Mann-Whitney test:  
949 non-significant.

950 SEM represented, independent biological repeats in supplementary file 2 and source data in  
951 supplementary file 1.

952

953 **Figure supplement 7 (related to Figure 3): Markers for age-dependent protein aggregation**

954 (A) Increased pharyngeal KIN-19 aggregation with age in animals expressing *Pkin-19::KIN-19::tagRFP*.

955 (B) Increased body-wall muscle KIN-19 aggregation with age in animals expressing *Pmyo-3::KIN-*  
956 *19::tagRFP*.

957 (C) Increased pharyngeal RHO-1 aggregation with age in animals expressing *Pmyo-2::RHO-1::tagRFP*.  
958 Already young adults display abundant RHO-1 aggregation.

959 (D) Absence of RHO-1 aggregation in the majority of animals expressing *Punc-54::RHO-1::Venus*.

960 Numbers of worms indicated in the bars. Significance calculated low + medium versus high aggregation  
961 levels compared to day 2 of adulthood; Fisher's exact test: \*\*p< 0.01, \*\*\*p< 0.001, \*\*\*\*p< 0.0001. See  
962 source data in supplementary file 1.

963 (E) RHO-1::tagRFP aggregates abundantly at day 2 compared to KIN-19::tagRFP. Fluorescent micrograph  
964 of the upper body region of animals expressing *Pkin-19::KIN-19::tagRFP* or *Pmyo-2::RHO-1::tagRFP*. Days  
965 of adulthood and exposure times displayed under images. Arrow heads highlight animals with high levels  
966 of KIN-19 aggregation in anterior bulb. Scale bar: 100  $\mu$ m



967 (F) KIN-19::tagRFP but not RHO-1::Venus aggregates in body-wall muscle (small puncta). Fluorescent  
968 micrograph of whole animals expressing *Punc-54::RHO-1::Venus* or *Pmyo-3::KIN-19::tagRFP*. Head region  
969 on the left. Days of adulthood and exposure times displayed under images. Scale bar: 200  $\mu$ m.

970

971 **Figure supplement 8 (related to Figure 3): KIN-19 aggregation in body-wall muscles impairs thrashing**

972 (A) KIN-19 aggregation in body-wall muscles impairs thrashing. Mean body bends per seconds are set to  
973 100% in *Pmyo-3::tagRFP* transgenics. Mann-Whitney test: \*\*\*\* $p < 0.0001$

974 (B) No effect on pumping detected in animals with mixed levels of KIN-19::tagRFP aggregation. N= 29-39  
975 animals analyzed per group. T-test: non-significant.

976 (C) Fluorescent tagRFP does not affect pharyngeal pumping in young animals. N= 26-27 animals analyzed  
977 per group. T-test: non-significant.

978 (D) Fluorescent tagRFP does not affect pharyngeal pumping in aged animals. N= 23-26 animals analyzed  
979 per group. T-test: non-significant.

980 SEM represented, independent biological repeats in supplementary file 2 and source data in  
981 supplementary file 1.

982

983 **Figure supplement 9 (related to Figure 3): KIN-19 and RHO-1 aggregation impacts muscle structure**

984 (A, B) Animals with KIN-19 aggregates show defective body-wall muscle structure at day 4. (A)  
985 Representative single-plane image showing wrinkled, thinner and faded actin filaments in the presence  
986 of KIN-19 aggregates. Top panel: F-actin staining with phalloidin (green). Bottom panel: Merged image  
987 with KIN-19 aggregates (magenta). Scale bar 30  $\mu$ m. (B) Quantification of the decline in body-wall muscle

988 structure with KIN-19 aggregation. Fisher's exact test: \*\*\*\*p< 0.0001. See source data in supplementary  
989 file 1.

990 (C, D) Animals with RHO-1 aggregates show defective pharyngeal muscle structure at day 2. (C)  
991 Representative single-plane image showing holes in the actin filaments in the presence of RHO-1  
992 aggregates. Top: merged view of pharynx (RHO-1::tagRFP, tagRFP in magenta and F-actin staining with  
993 phalloidin in green); Bottom: zoom into boxed area. Scale bar: 15  $\mu\text{m}$ , zoom: 3  $\mu\text{m}$ . (D) Quantification of  
994 defective pharyngeal muscle structure with RHO-1 aggregation. Fisher's exact test: \*\*\*\*p< 0.0001. See  
995 source data in supplementary file 1.

996

997 Supplementary file 1: source data

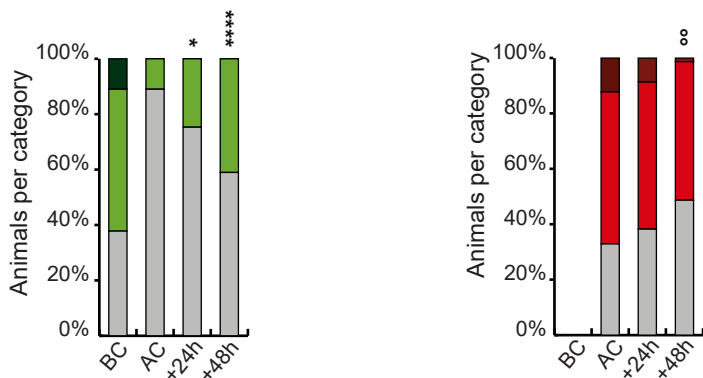
998 Supplementary file 2: Pharyngeal pumping and thrashing repeats

999 Supplementary file 3: parameters for thrashing analysis

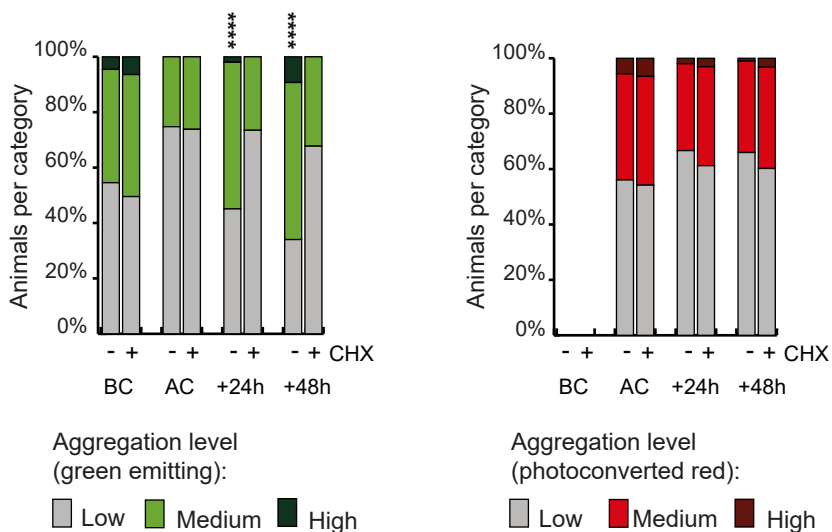
1000

# Figure 1

## A Body-wall muscle KIN-19::mEOS2 aggregation



## B Pharyngeal KIN-19::mEOS2 aggregation



## C Pharyngeal KIN-19::mEOS2 Day 7, 24h after conversion

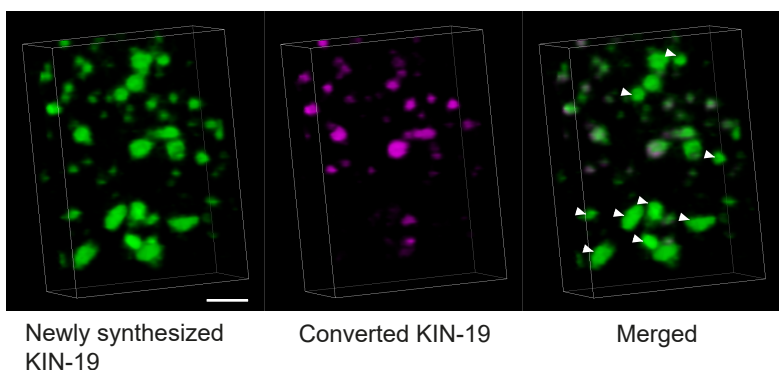
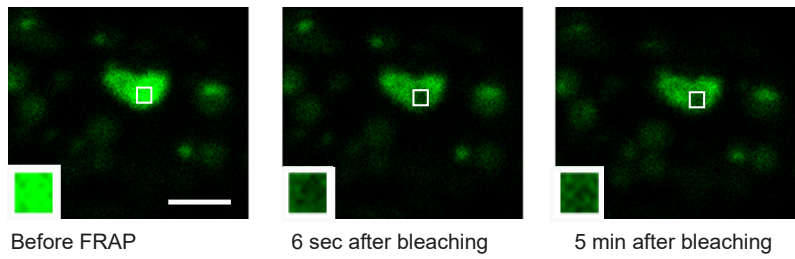
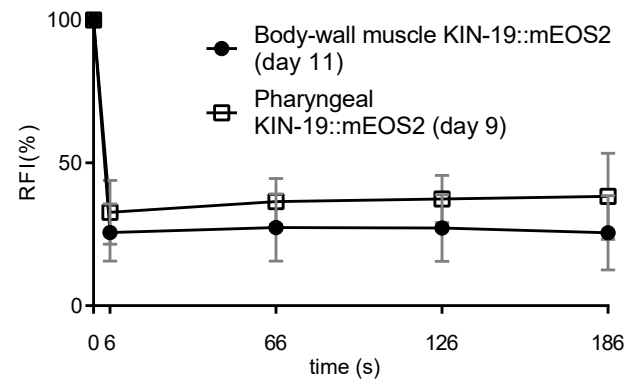


# Figure supplement 1

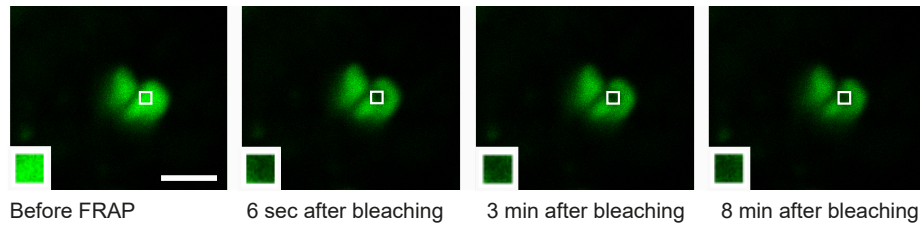
## A KIN-19::mEOS2 expressed in the body wall muscle



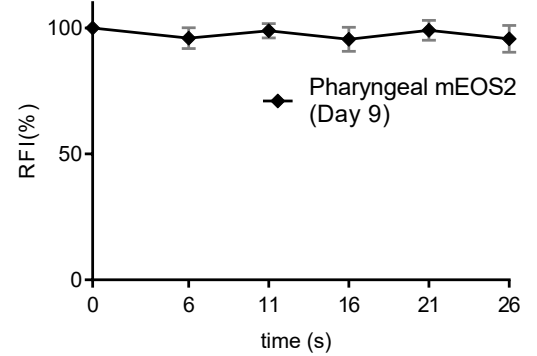
## C



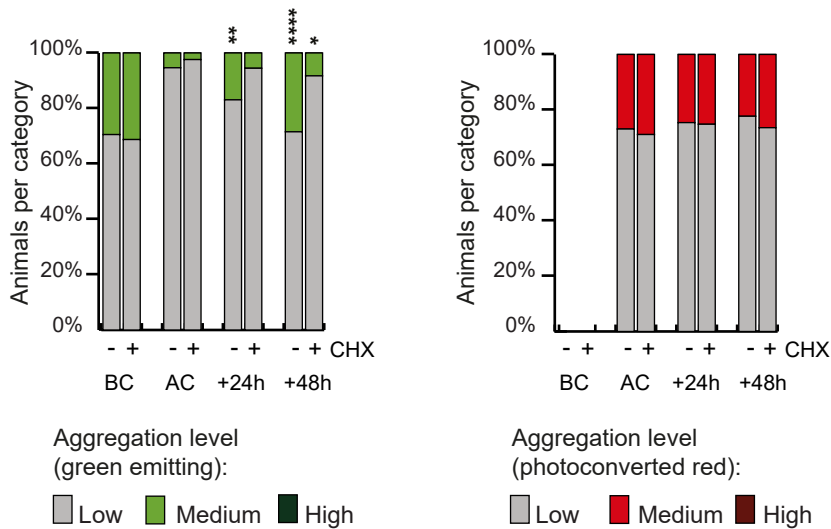
## B KIN-19::mEOS2 expressed in the pharynx



## D



## E Pharyngeal KIN-19::mEOS2 aggregation, photoconversion at day 2



## F RHO-1::mEOS2 expressed in the pharynx at day 1, 24h after photoconversion

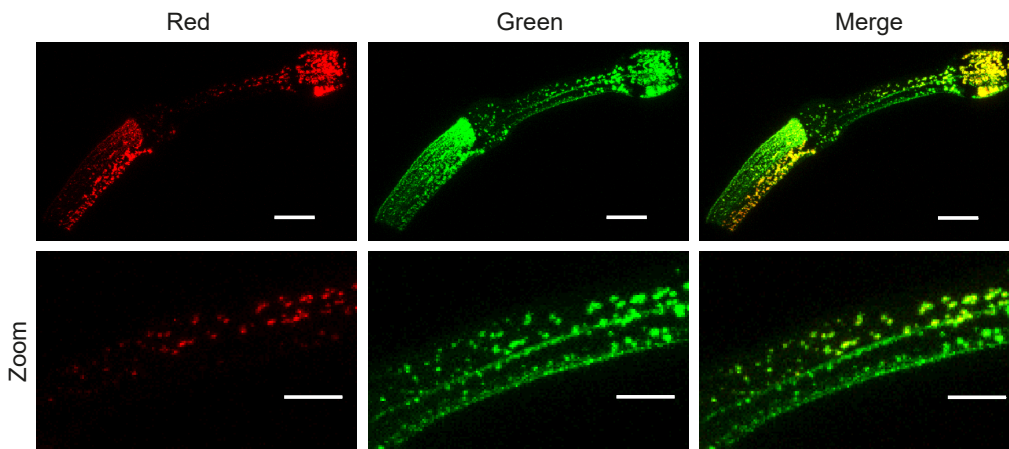
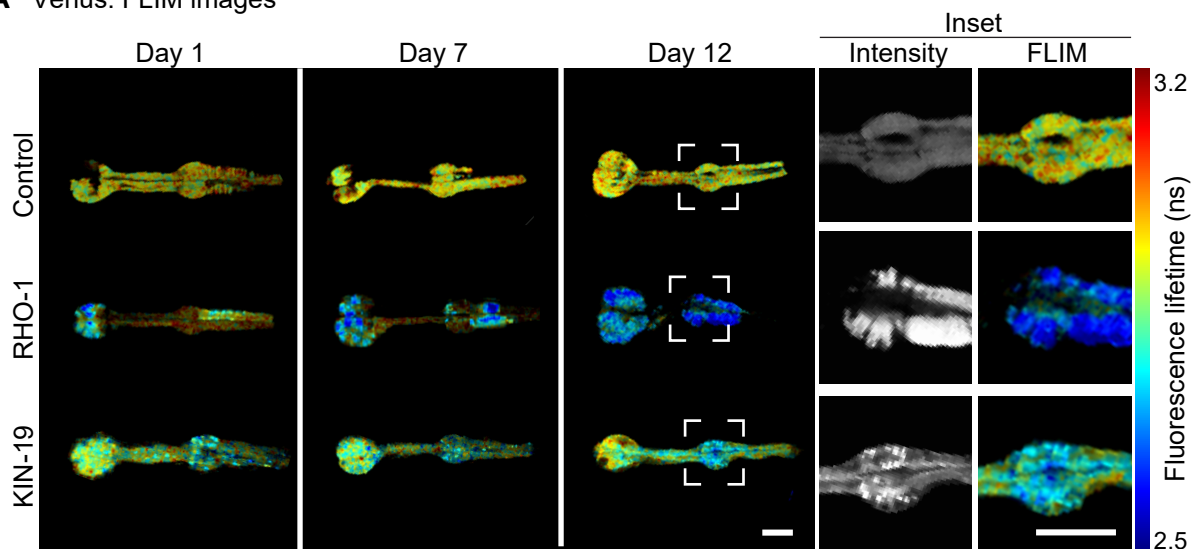
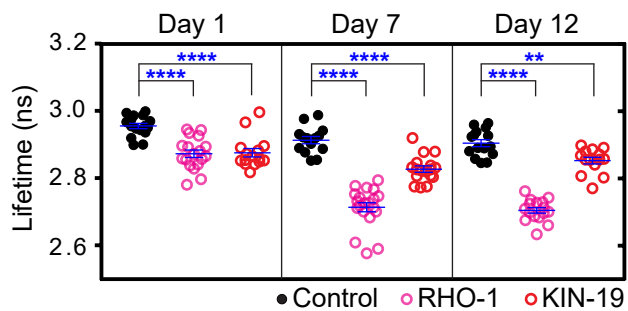


Figure 2

**A** Venus: FLIM images



**B** Venus: fluorescence lifetimes



**C** Venus: Day 12 histograms

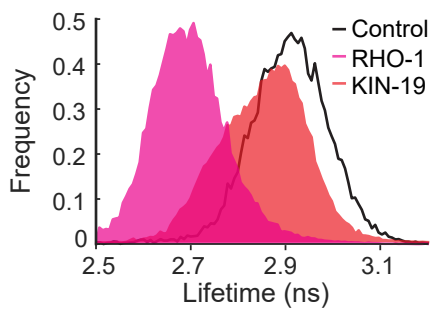
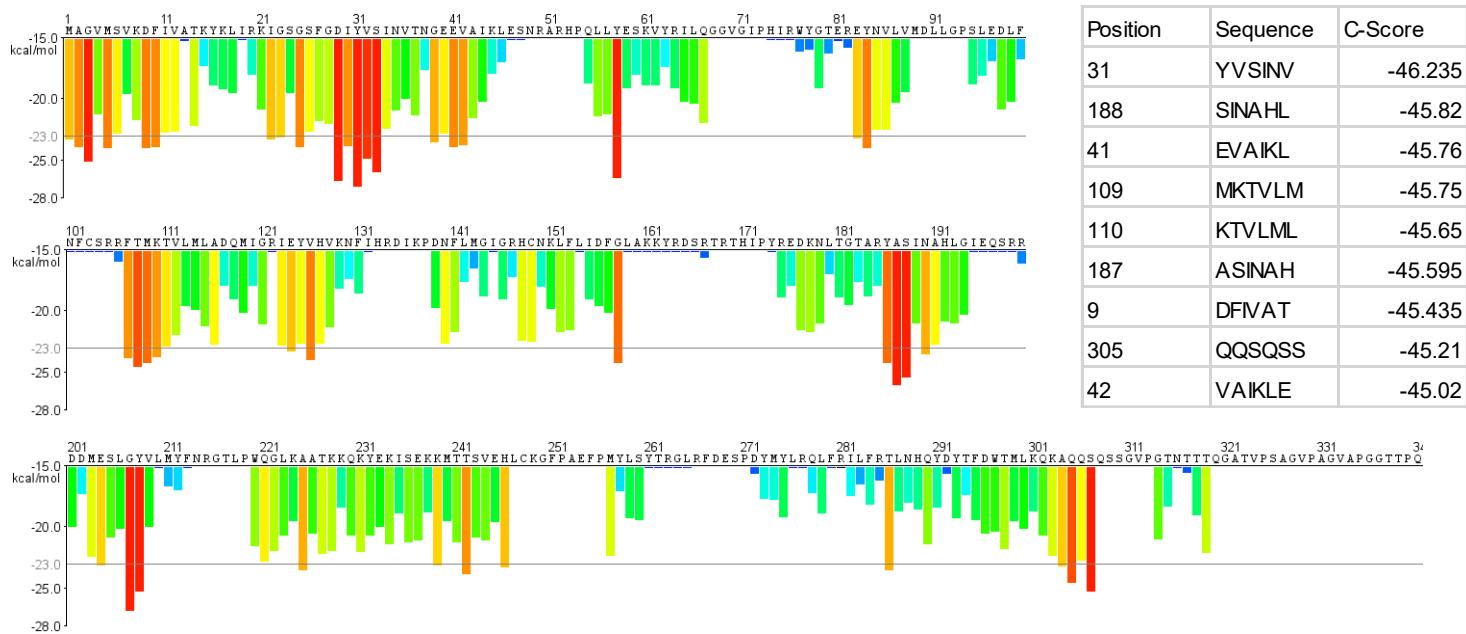


# Figure supplement 2

## A Fibrillation Propensity profile for KIN-19



## B Fibrillation Propensity profile for RHO-1

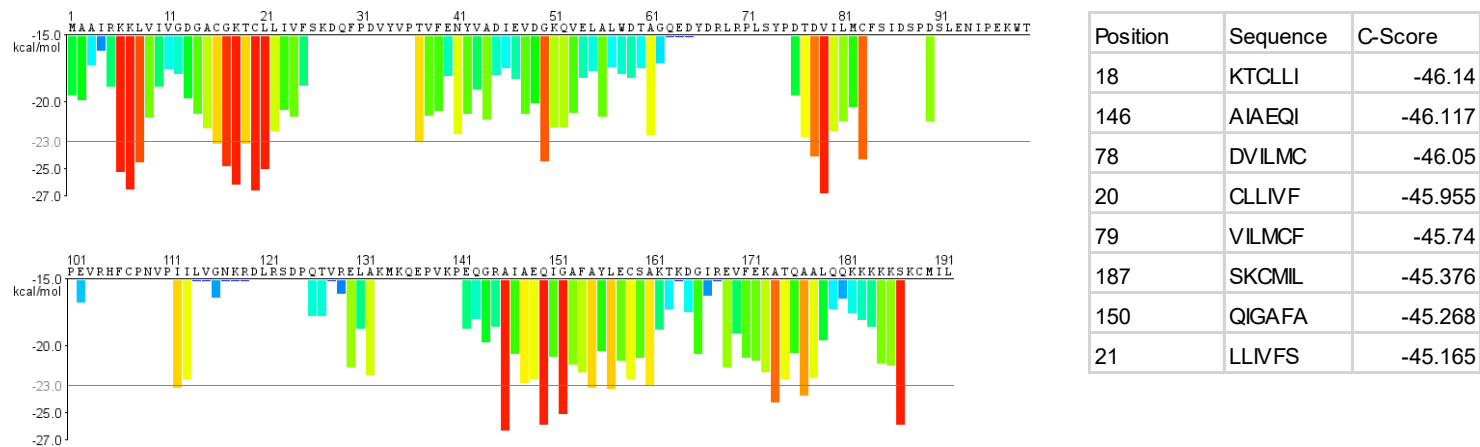
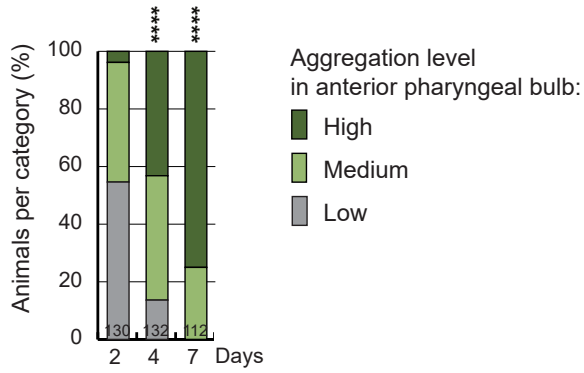
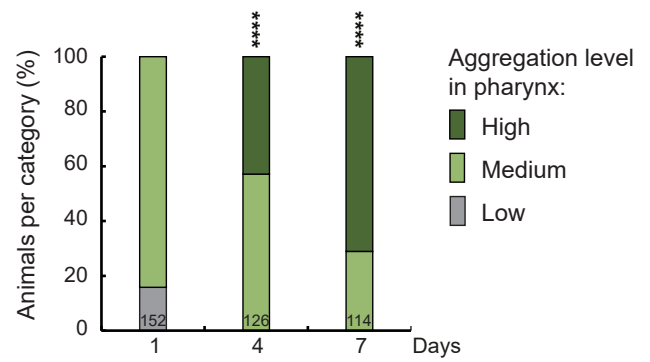


Figure supplement 3

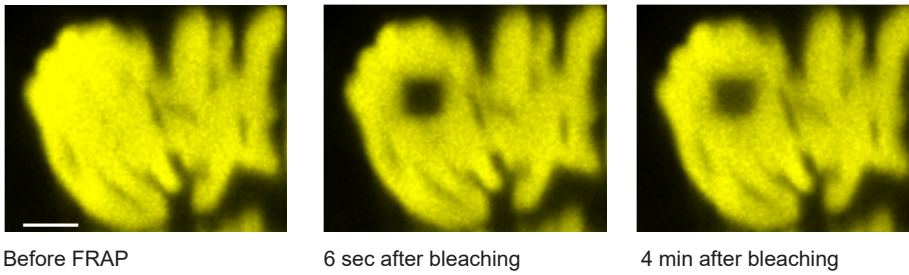
**A** Pharyngeal KIN-19::Venus aggregation



**B** Pharyngeal RHO-1::Venus aggregation



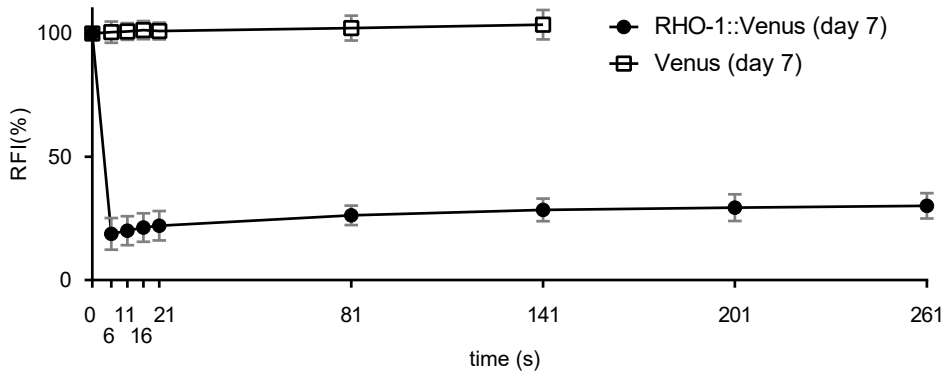
**C** RHO-1::Venus expressed in the pharynx, day 7



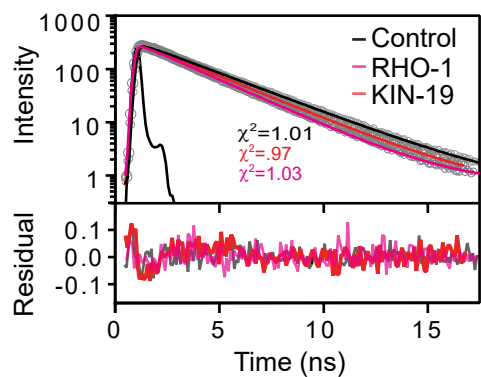
**D**

RHO-1::Venus				
Days of adulthood	Number of animals	Puncta evaluated	Immobile (no recovery)	Mobile (recovery)
1	5	11	11	0
7	5	10	10	0
11	6	11	11	0
14	5	10	10	0

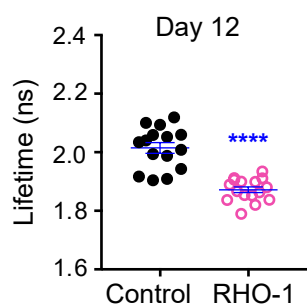
**E**



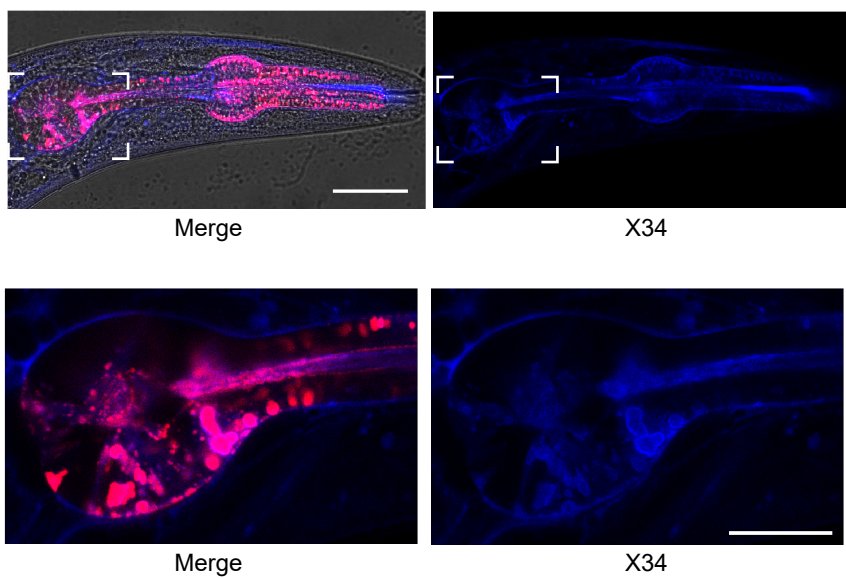
**A** Venus: fluorescence lifetime fits



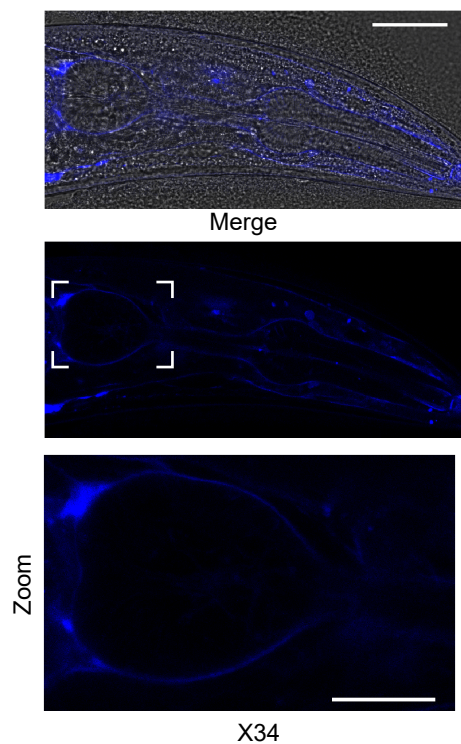
**B** TagRFP: fluorescence lifetimes



**C** Pharyngeal RHO-1::tagRFP with X34 staining



**D** Wild-type with X34 staining



**E** Pharyngeal RHO-1::tagRFP with X34 staining

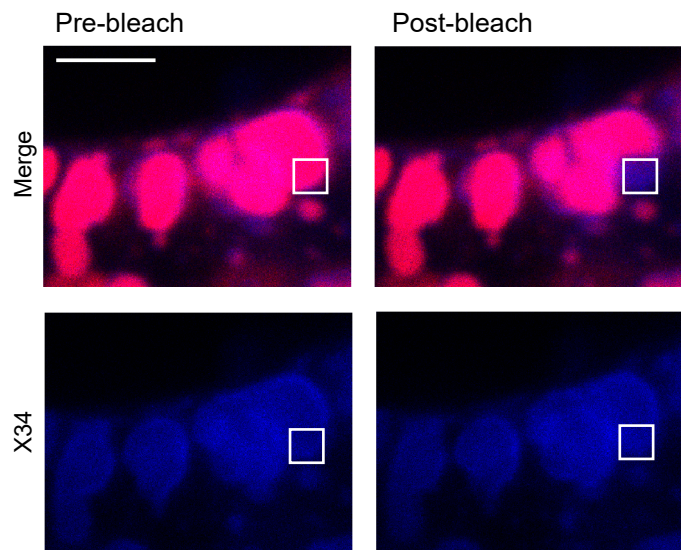




Figure supplement 5

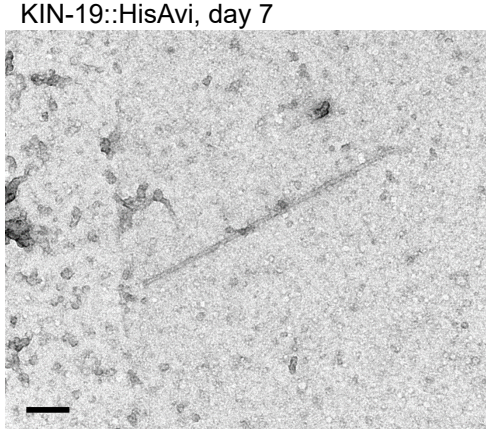
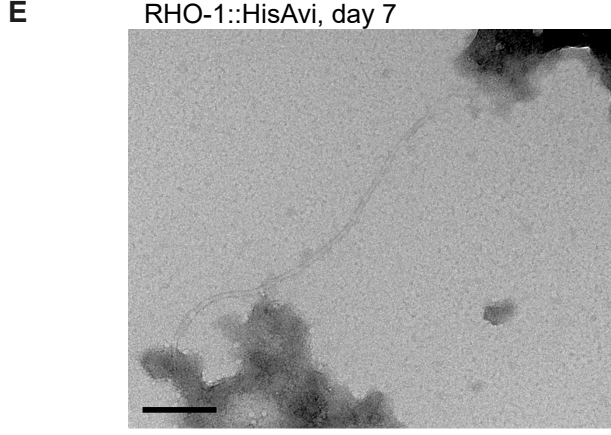
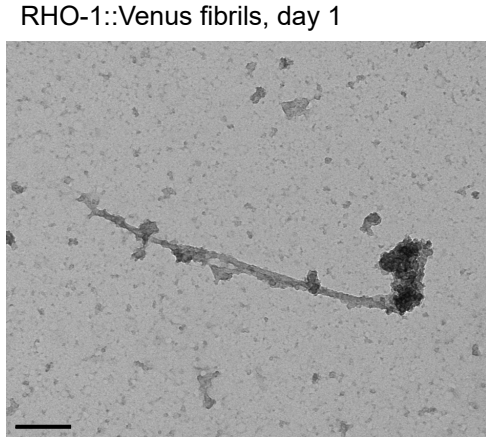
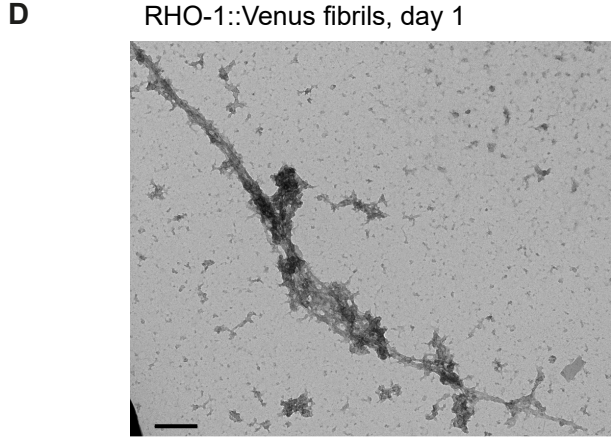
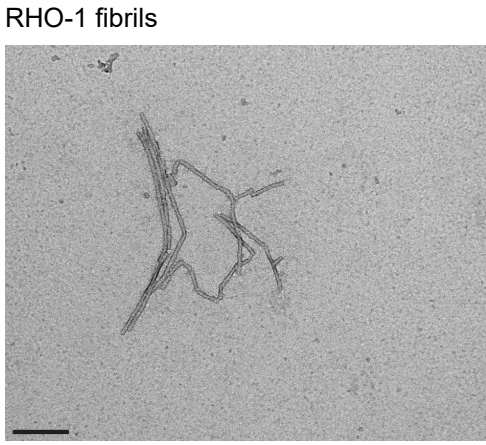
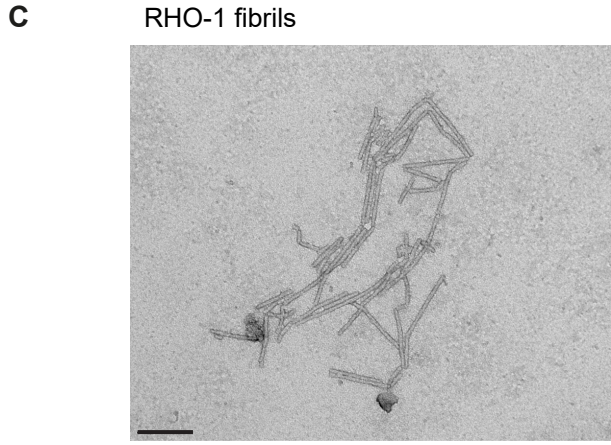
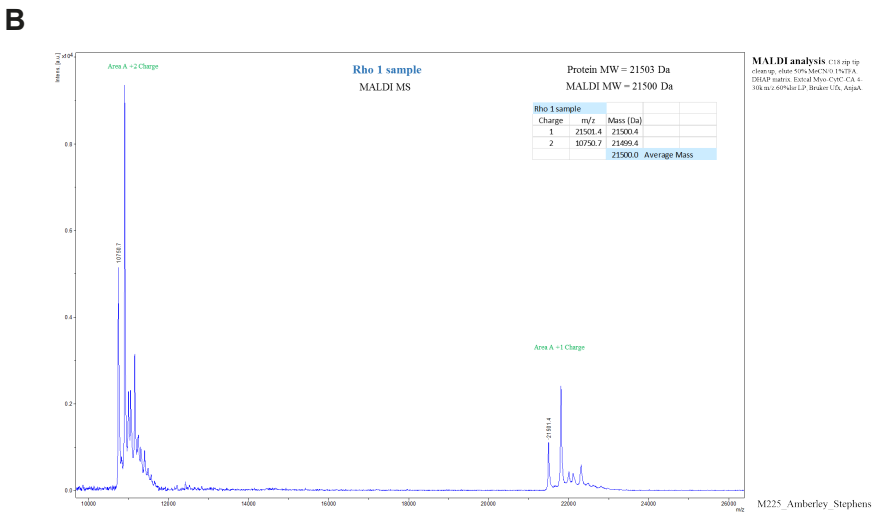
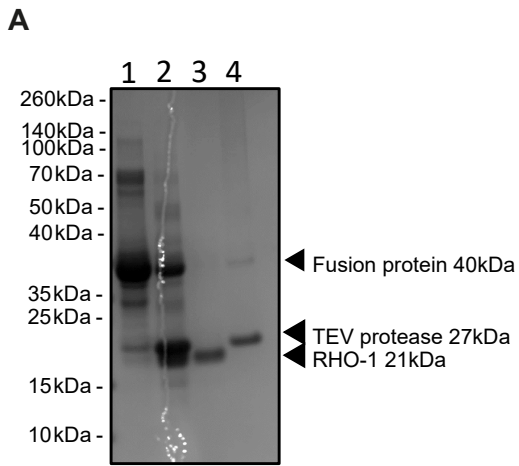
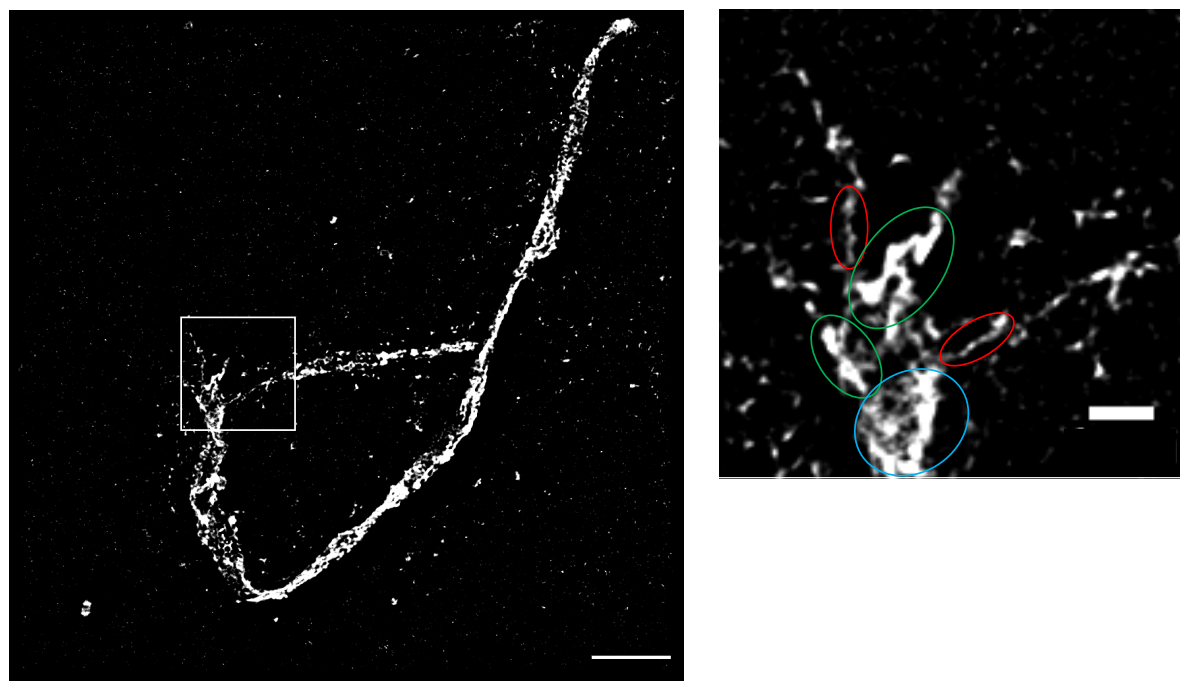


Figure supplement 6

**A** ThT staining of fibrils (RHO-1::HisAvi, day 7)



**B** ThT staining of fibrils

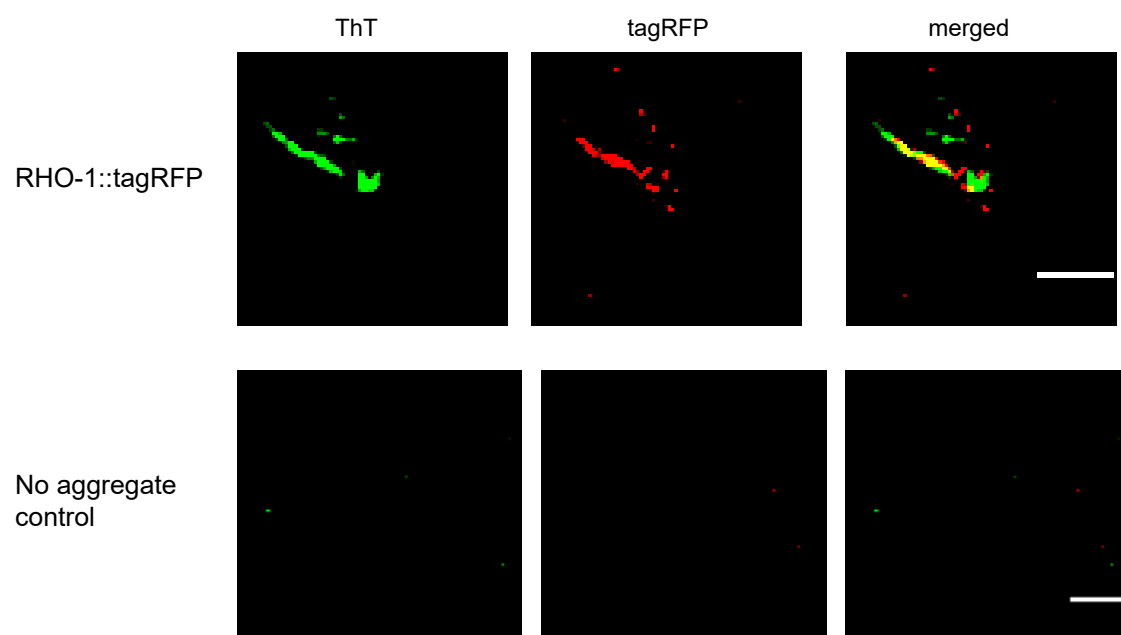
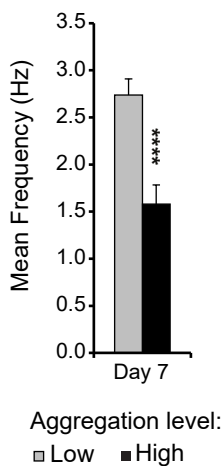
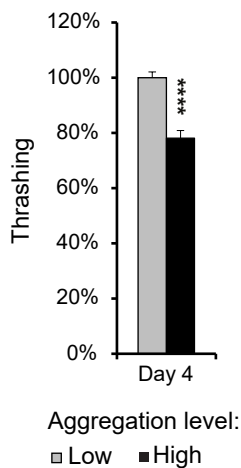


Figure 3

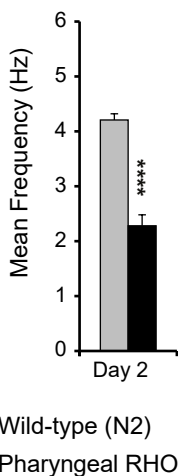
**A** Pumping  
Pharyngeal KIN-19::tagRFP



**B** Thrashing  
Body-wall muscle KIN-19::tagRFP



**C** Pumping  
Pharyngeal RHO-1::tagRFP



**D** Thrashing  
Body-wall muscle RHO-1::Venus  
(no aggregation)

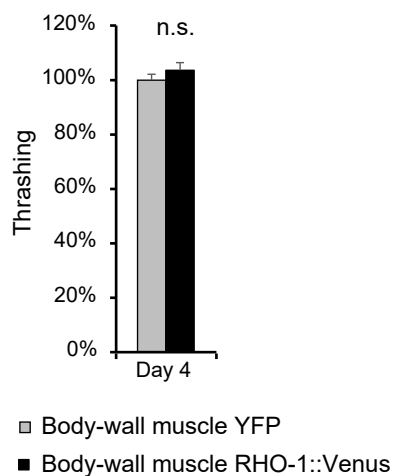
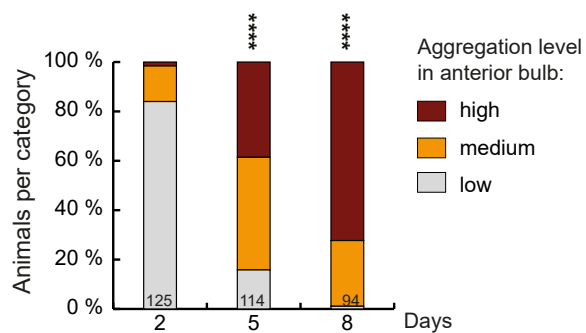
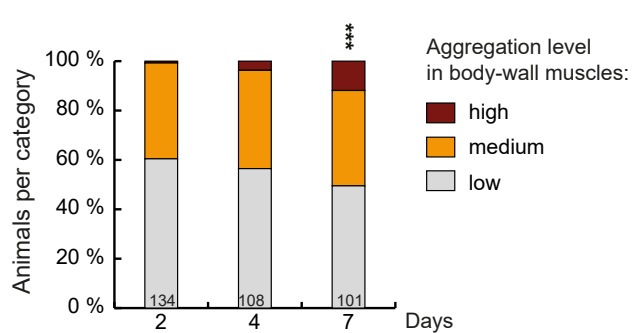


Figure supplement 7

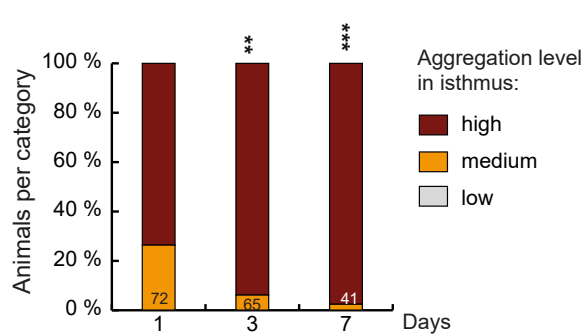
**A** Pharyngeal KIN-19::tagRFP aggregation



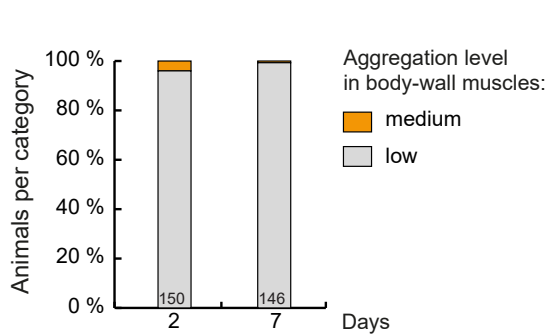
**B** Body-wall muscle KIN-19::tagRFP aggregation



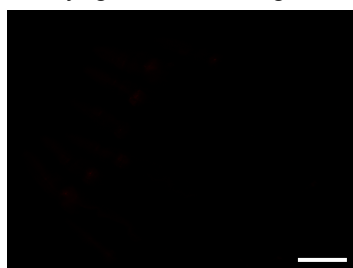
**C** Pharyngeal RHO-1::tagRFP aggregation



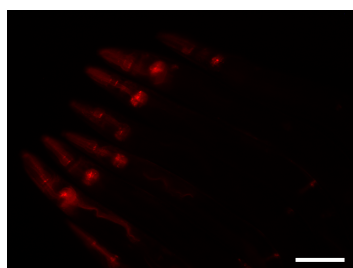
**D** Body-wall muscle RHO-1::venus aggregation



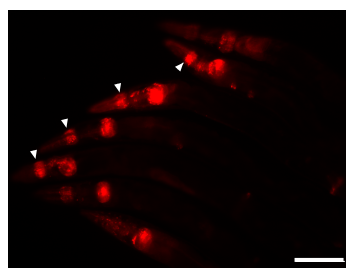
**E** Pharyngeal KIN-19::tagRFP



Day 2; 50ms

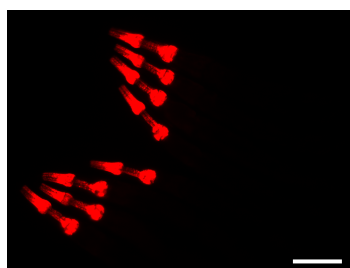


Day 2; 500ms

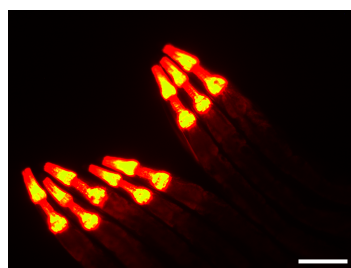


Day 7; 500ms

Pharyngeal RHO-1::tagRFP

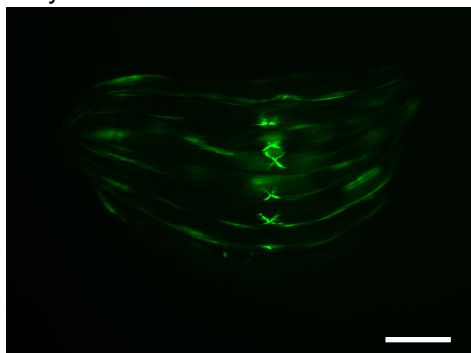


Day 2; 50ms



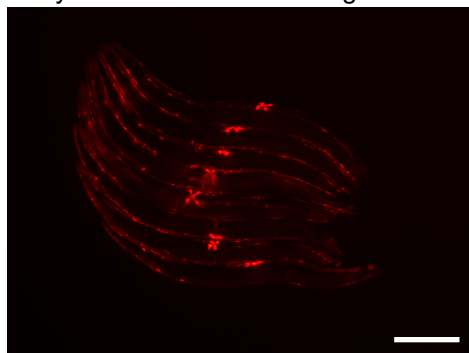
Day 2; 500ms

**F** Body-wall muscle RHO-1::venus

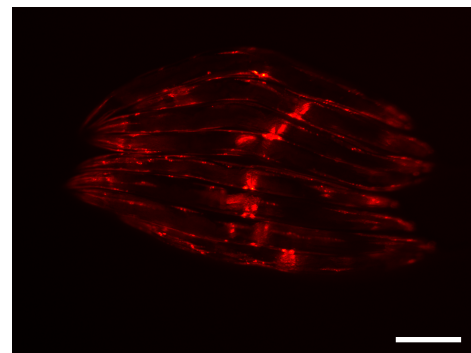


Day 2; exposure: 1s

Body-wall muscle KIN-19::tagRFP



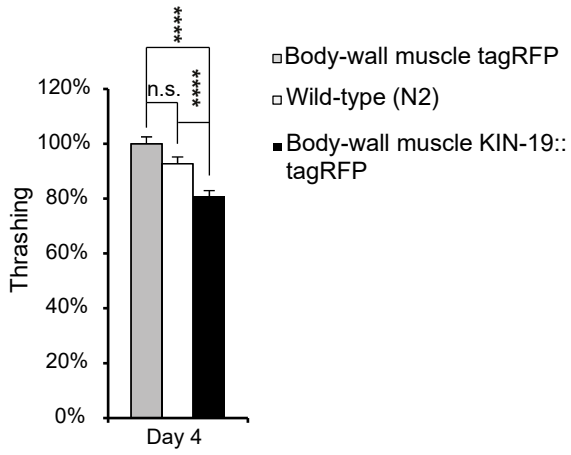
Day 2; exposure: 1s



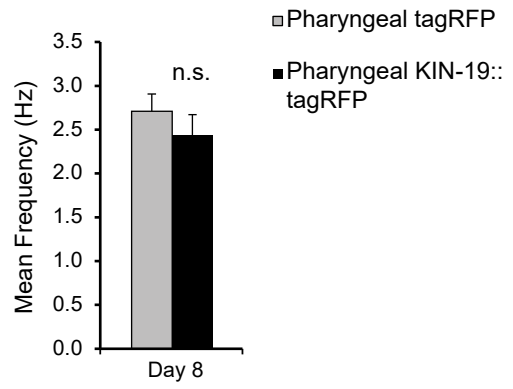
Day 4; exposure: 1s

# Figure supplement 8

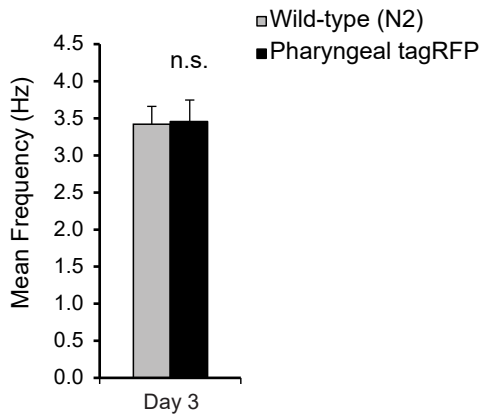
## A Thrashing with body-wall muscle KIN-19::tagRFP



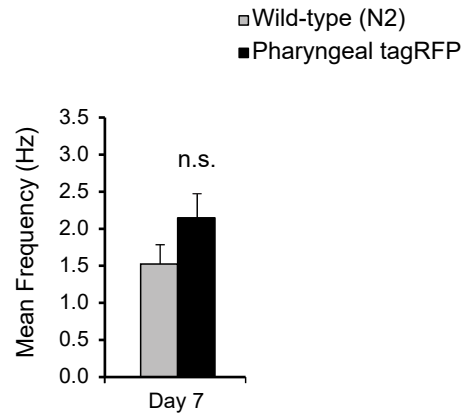
## B Pumping with pharyngeal KIN-19::tagRFP



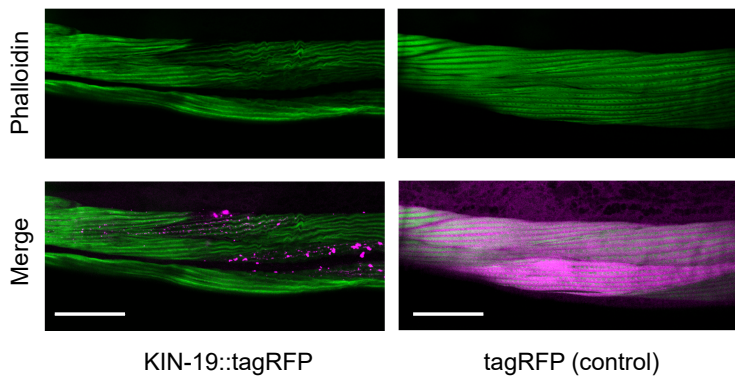
## C Pumping with pharyngeal tagRFP



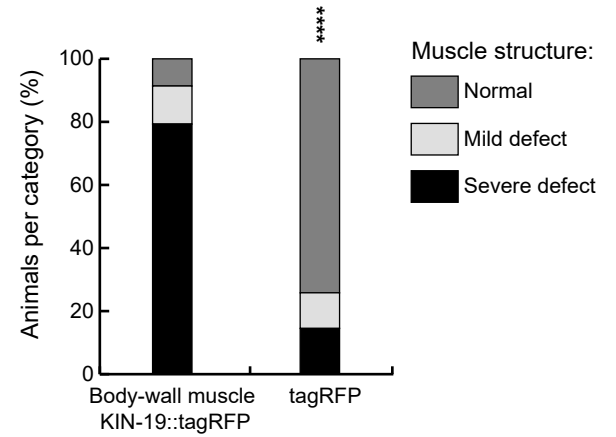
## D Pumping with pharyngeal tagRFP



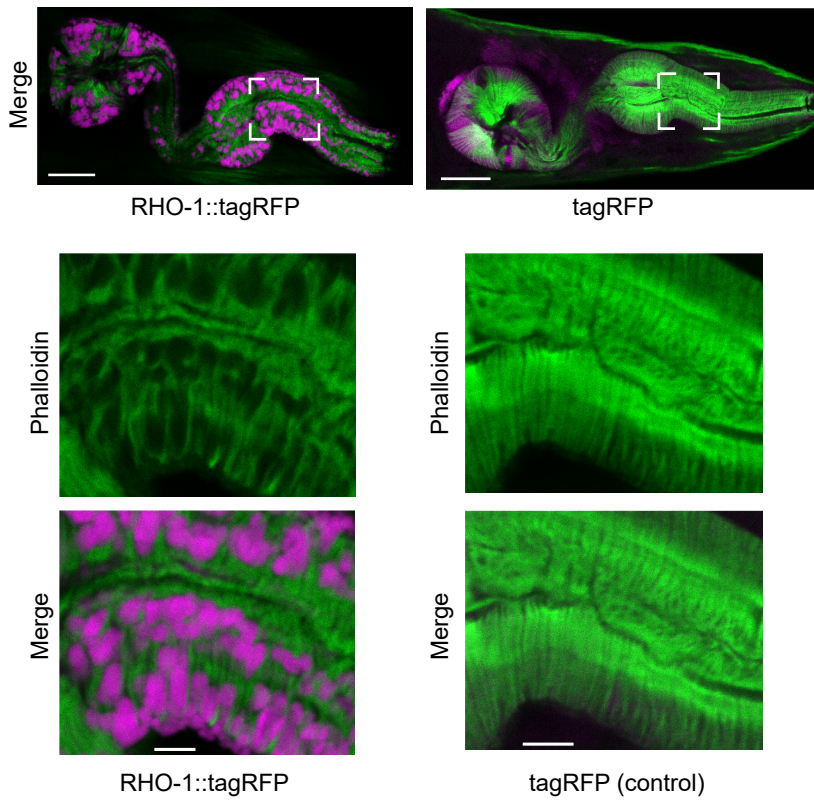
**A** F-actin staining in body-wall muscles



**B** Quantitative analysis of F-actin in body-wall muscles



**C** F-actin staining in pharyngeal muscles



**D** Quantitative analysis of F-actin in pharyngeal muscles

